



HAL
open science

Abrupt excursions in water vapor isotopic variability at the Pointe Benedicte observatory on Amsterdam Island

Amaelle Landais, Cécile Agosta, Françoise Vimeux, Olivier Magand, Cyrielle Solis, Alexandre Cauquoin, Niels Dutrievoz, Camille Risi, Christophe Leroy-dos Santos, Elise Fourré, et al.

► **To cite this version:**

Amaelle Landais, Cécile Agosta, Françoise Vimeux, Olivier Magand, Cyrielle Solis, et al.. Abrupt excursions in water vapor isotopic variability at the Pointe Benedicte observatory on Amsterdam Island. *Atmospheric Chemistry and Physics*, 2024, 24 (8), pp.4611 - 4634. 10.5194/acp-24-4611-2024 . hal-04573105

HAL Id: hal-04573105

<https://hal.science/hal-04573105v1>

Submitted on 13 May 2024

HAL is a multi-disciplinary open access archive for the deposit and dissemination of scientific research documents, whether they are published or not. The documents may come from teaching and research institutions in France or abroad, or from public or private research centers.

L'archive ouverte pluridisciplinaire **HAL**, est destinée au dépôt et à la diffusion de documents scientifiques de niveau recherche, publiés ou non, émanant des établissements d'enseignement et de recherche français ou étrangers, des laboratoires publics ou privés.



Abrupt excursions in water vapor isotopic variability at the Pointe Benedicte observatory on Amsterdam Island

Amaelle Landais¹, Cécile Agosta¹, Françoise Vimeux^{1,2}, Olivier Magand³, Cyrielle Solis¹, Alexandre Cauquoin⁴, Niels Dutrievoz¹, Camille Risi⁵, Christophe Leroy-Dos Santos¹, Elise Fourré¹, Olivier Cattani¹, Olivier Jossoud¹, Bénédicte Minster¹, Frédéric Prié¹, Mathieu Casado¹, Aurélien Dommergue⁶, Yann Bertrand⁶, and Martin Werner⁷

¹Laboratoire des Sciences du Climat et de l'Environnement, LSCE/IPSL, CEA-CNRS-UVSQ, Université Paris-Saclay, 91191 Gif-sur-Yvette, France

²HydroSciences Montpellier (HSM), UMR 5569 (UM, CNRS, IRD), 34095 Montpellier, France

³Observatoire des Sciences de l'Univers de La Réunion (OSU-Réunion), UAR 3365, Université de La Réunion, CNRS, IRD, Météo France, Saint-Denis, La Réunion, France

⁴Institute of Industrial Science (IIS), The University of Tokyo, Kashiwa, Japan

⁵Laboratoire de Météorologie Dynamique, Institut Pierre – Simon Laplace, Sorbonne Université/CNRS/École Polytechnique – IPP, Paris, France

⁶Univ. Grenoble Alpes, CNRS, INRAE, IRD, Grenoble INP^T, IGE, 38000 Grenoble, France

⁷Alfred Wegener Institute, Helmholtz Centre for Marine and Polar Research, 27570 Bremerhaven, Germany

Correspondence: Amaelle Landais (amaelle.landais@lsce.ipsl.fr) and Cécile Agosta (cecile.agosta@lsce.ipsl.fr)

Received: 14 July 2023 – Discussion started: 22 August 2023

Revised: 22 February 2024 – Accepted: 23 February 2024 – Published: 18 April 2024

Abstract. In order to complement the picture of the atmospheric water cycle in the Southern Ocean, we have continuously monitored water vapor isotopes since January 2020 on Amsterdam Island in the Indian Ocean. We present here the first 2-year long water vapor isotopic record at this site. We show that the water vapor isotopic composition largely follows the water vapor mixing ratio, as expected in marine boundary layers. However, we detect 11 periods of a few days where there is a strong loss of correlation between water vapor $\delta^{18}\text{O}$ and water vapor mixing ratio as well as abrupt negative excursions of water vapor $\delta^{18}\text{O}$. These excursions often occur toward the end of precipitation events. Six of these events show a decrease in gaseous elemental mercury, suggesting subsidence of air from a higher altitude.

Our study aims to further explore the mechanism driving these negative excursions in water vapor $\delta^{18}\text{O}$. We used two different models to provide a data–model comparison over this 2-year period. While the European Centre Hamburg model (ECHAM6-wiso) at 0.9° was able to reproduce most of the sharp negative water vapor $\delta^{18}\text{O}$ excursions, hence validating the physics process and isotopic implementation in this model, the Laboratoire de Météorologie Dynamique Zoom model (LMDZ-iso) at 2° (3°) resolution was only able to reproduce seven (one) of the negative excursions, highlighting the possible influence of the model resolution for the study of such abrupt isotopic events. Based on our detailed model–data comparison, we conclude that the most plausible explanations for such isotopic excursions are rain–vapor interactions associated with subsidence at the rear of a precipitation event.

1 Introduction

The main sources of uncertainty in the atmospheric components of Earth system models for future climate projections are associated with complex atmospheric processes, particularly those related to water vapor and clouds (Arias et al., 2021; Sherwood et al., 2014). Decreasing these uncertainties is of vital interest as the hydrological cycle is a fundamental element of the climate system because it allows us, via the transport of water vapor, to ensure Earth's thermal balance.

Stable water isotopes are a useful tool for studying the influence of dynamical processes on the water budget at various spatial and temporal scales. They provide a framework for analyzing moist processes over a range of timescales from large-scale moisture transport to cloud formation, precipitation, and small-scale turbulent mixing (Bailey et al., 2023; Dahinden et al., 2021; Galewsky et al., 2016; Thurnherr et al., 2020).

The relative abundance of heavy and light isotopes in different water reservoirs is altered during phase change processes due to isotopic fractionation (caused by a difference in saturation vapor pressure and molecular diffusivity in the air and the ice). Each time a phase change occurs, the relative abundance of water vapor isotopes is altered. We express the abundance of the heavy isotopes D and ^{18}O with respect to the number of light isotopes H and ^{16}O , respectively, in the water molecules through the notation δ :

$$\delta^{18}\text{O} = \left(\frac{(^{18}\text{O}/^{16}\text{O})_{\text{Sample}}}{(^{18}\text{O}/^{16}\text{O})_{\text{VSMOW}}} - 1 \right) \times 1000, \quad (1)$$

$$\delta\text{D} = \left(\frac{(D/H)_{\text{Sample}}}{(D/H)_{\text{VSMOW}}} - 1 \right) \times 1000, \quad (2)$$

where $(^{18}\text{O}/^{16}\text{O})$ and (D/H) represent the isotopic ratios of oxygen and hydrogen atoms in water and VSMOW (Vienna Standard Mean Ocean Water) is an international reference standard for water isotopes.

There are two types of isotopic fractionation: equilibrium fractionation, which is caused by the difference in saturation vapor pressure of different isotopes, and non-equilibrium fractionation, which occurs due to molecular diffusion (e.g., during ocean evaporation in an undersaturated atmosphere or snowflake condensation in an oversaturated atmosphere). In the water vapor above the ocean, the proportion of non-equilibrium fractionation and hence diffusive processes can be estimated by the deuterium excess, a second-order isotopic variable denoted “d-excess” and defined as (Dansgaard, 1964)

$$\text{d-excess} = \delta\text{D} - 8 \times \delta^{18}\text{O}. \quad (3)$$

In recent years and thanks to the development of optical spectroscopy enabling continuous measurements of water isotope ratios in water vapor, an increasing number of studies have focused on the use of water vapor stable isotopes

to document the dynamics of the water cycle over synoptic weather events, such as cyclones, cold fronts, atmospheric rivers (Aemisegger et al., 2015; Ansari et al., 2020; Bhattacharya et al., 2022; Dütsch et al., 2016; Graf et al., 2019; Lee et al., 2019; Munksgaard et al., 2015; Tremoy et al., 2014), or water cycle processes such as evaporation over the ocean or deep convection (Benetti et al., 2015; Bonne et al., 2019). Several instruments have been installed either at observatory stations (e.g., Aemisegger et al., 2012; Guilpart et al., 2017; Leroy-Dos Santos et al., 2020; Steen-Larsen et al., 2013; Tremoy et al., 2012), on boats (e.g., Benetti et al., 2014; Thurnherr et al., 2020), or on aircraft (Henze et al., 2022). In the aforementioned studies, the interpretation of the isotopic records is often performed using a hierarchy of isotopic models, from conceptual models (Rayleigh type) to general circulation models or regional weather prediction models equipped with water isotopes (Ciais and Jouzel, 1994; Markle and Steig, 2022; Risi et al., 2010; Werner et al., 2011). Such data comparisons enable one to test the performances of the models either in the simulation of the dynamics of the atmospheric water cycle or in the implementation of the water isotopes. Our study is part of these dynamics analyses and aims at improving the documentation of the climate and atmospheric water cycle in the southern Indian Ocean, a region which has been poorly documented until now.

Over the previous years, we installed three water vapor analyzers on La Réunion at the Maïdo observatory (21.079° S, 55.383° E; 2160 m) (Guilpart et al., 2017) and in Antarctica (Dumont d'Urville – 66.663° S, 140° E; 202 m; Concordia – 75.1° S, 123.333° E; 3233 m; Bréant et al., 2019; Casado et al., 2016; Leroy-Dos Santos et al., 2021). These instruments have been used for the following purposes. They document the diurnal variability of the isotopic signal with the influence of the subtropical westerly jet on the water isotopic signal at night as well as the cyclonic activity on La Réunion. In Antarctica, the records have shown a strong influence of katabatic winds on the isotopic composition of water vapor (Bréant et al., 2019). In order to complete the picture of the atmospheric water cycle over the Indian basin of the Southern Ocean already measured by these three analyzers, we installed a new water vapor isotopic analyzer at mid-latitude in the southern Indian Ocean on Amsterdam Island (Fig. 1) in November 2019. Amsterdam Island is one of the very rare atmospheric observatories in the Southern Hemisphere. Moreover, the southern Indian Ocean is a significant moisture source of Antarctic precipitation, notably in the region encompassing the Dumont d'Urville and Concordia stations (Jullien et al., 2020; Wang et al., 2020).

The objective of this study is to provide the first analyses of isotopic records (vapor and precipitation) on Amsterdam Island, with a comparison of meteorological data and environmental data collected in parallel at the Amsterdam Island observatory (e.g., atmospheric mercury) to help with the interpretation of isotopic records. Indeed, previous stud-

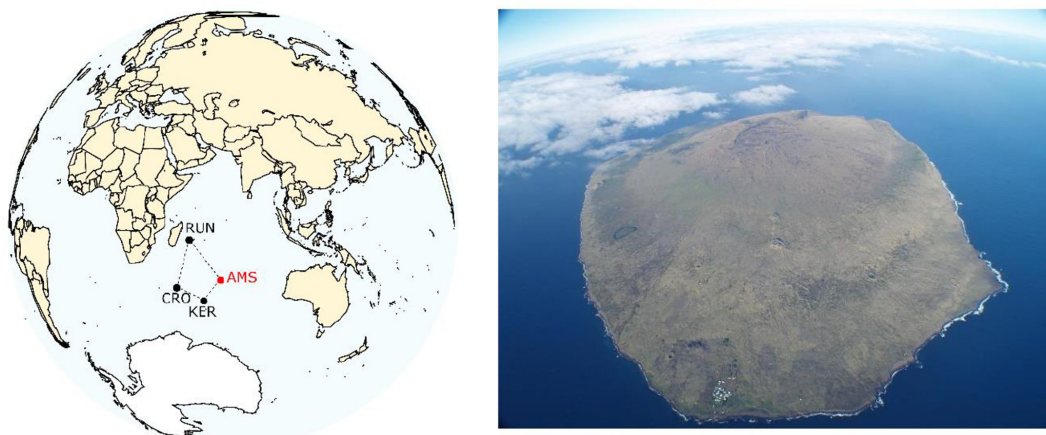


Figure 1. Location (left) and picture (right) of Amsterdam Island. CRO: Crozet islands; RUN: La Réunion; KER: Kerguelen island; AMS: Amsterdam Island. Picture credit: left – from Olivier Magand adapted from Angot et al. (2016); right – photo taken by Olivier Magand.

ies have shown that gaseous elemental mercury decreases with increasing altitude in marine environments, suggesting that gaseous elemental mercury can be used as a tracer of subsidence of air from high altitudes (e.g., Koenig et al., 2023). This study includes analyses of meteorological maps, back trajectories, and outputs from general circulation models equipped with water isotopes. After a description of the different records over the years 2020 and 2021, model simulations, and back trajectories, we focus on some low-pressure events associated with a strong negative excursion of $\delta^{18}\text{O}_v$ over a few days and a decoupling between $\delta^{18}\text{O}_v$ and humidity. These events are then used for evaluation of atmospheric components of Earth system models equipped with water isotopes.

2 Methods

2.1 Site

Labeled a global site for the Global Atmosphere Watch World Meteorological Organization, Amsterdam Island (37.7983°S , 77.5378°E) is a remote and very small island of 55 km^2 with a population of about 30 residents, located in the southern Indian Ocean at 3300 and 4200 km downwind from the nearest countries, Madagascar and South Africa, respectively (Sprovieri et al., 2016). The climate is temperate and generally mild with frequent presence of clouds (the average total sunshine hours is 1581 hr^{-1} over the period 1981–2010 from Météo-France data). Seasonal boundaries are defined as follows: winter from July to September and summer from December to February, in line with previous studies (Sciare et al., 2009). The average temperature is lower in winter compared to summer (10.5°C vs. 15°C), while the relative humidity and wind speed remain high (50%–85% and 5 m s^{-1} – 15 m s^{-1} , respectively) most of the year without a clear seasonal cycle.

Numerous atmospheric compounds and meteorological parameters are and have been continuously monitored at the site since 1960 (Angot et al., 2014; El Yazidi et al., 2018; Gaudry et al., 1983; Gros et al., 1999, 1998; Polian et al., 1986; Sciare et al., 2000, 2009; Slemr et al., 2015, 2020). In particular, the Amsterdam Island (AMS) site hosts several dedicated atmospheric observation instruments, notably at the Pointe Bénédicte atmospheric observatory (70 m above sea level), where greenhouse gas concentrations and mercury (Hg) are monitored. Hg species have been continuously measured since 2012.

2.2 Long-term measurements

2.2.1 Meteorological measurements

One meteorological station has been installed at the top of an observation mast (25 m above ground level, hence 95 m above sea level) at the Pointe Bénédicte observatory since 1980 (data used during this study). Wind speed and direction, atmospheric pressure, air temperature, and relative humidity data are currently obtained at 1 min resolution. Another meteorological station is based on the island and is operated by Météo-France at Martin-de-Viviès life base around 27 m above sea level and about 2 km east of the Pointe Bénédicte observatory collecting air temperature, humidity, precipitation, wind speed and direction, pressure, and solar radiation.

2.2.2 Gaseous elemental mercury (GEM)

Atmospheric GEM measurements have been conducted since 2012 in the framework of the IPEV GMOS_{Stral}-1028 observatory program at the Pointe Bénédicte atmospheric research facility (Magand et al., 2022). GEM is continuously measured (15 min data frequency acquisition) using a Tekran 2537 A/B instrument model (Angot et al., 2014; Li et al., 2023; Slemr et al., 2015, 2020; Sprovieri et al., 2016). The

measurement is based on mercury enrichment on a gold cartridge, followed by thermal desorption and detection by cold vapor atomic fluorescence spectroscopy (Bloom and Fitzgerald, 1988; Fitzgerald and Gill, 1979). Concentrations are expressed in nanograms per cubic meter under standard temperature and pressure conditions (273.15 K and 1013.25 hPa) with an instrumental detection limit below 0.1 ng m^{-3} and a GEM average uncertainty value around 10 % (Slemr et al., 2015). The instrument is automatically calibrated following a strict procedure adapted from that of Dumarey et al. (1985). Ambient air is sampled at 1.2 L min^{-1} through a heated (50°C) and UV-protected PTFE (polytetrafluoroethylene) sampling line, with an inlet installed outside, 6 m above ground level (76 m above sea level). The air is filtered through two $0.45 \mu\text{m}$ pore size polyethersulfone and one PTFE 47 mm diameter filters before entering in Tekran to prevent the introduction of any particulate material into the detection system as well as to capture any gaseous oxidized mercury or particulate-bound mercury species, ensuring that only GEM is sampled. To ensure the comparability of mercury measurements around the world, the instrument is operated according to the Global Mercury Observation System standard operating procedures (Sprovieri et al., 2016; Steffen et al., 2012).

In this study, and even though long-range transport and a variable tropopause height may modulate the signal, atmospheric GEM is used as a potential tracer of stratosphere-to-troposphere intrusion and/or subsidence of upper-tropospheric air (above 5–6 km), which may impact the atmospheric records at the Pointe Benedicte observatory, where marine boundary layer air is collected most of the time (Angot et al., 2014; Slemr et al., 2015, 2020; Sprovieri et al., 2016). Mercury in the atmosphere consists of three forms: GEM as defined above, gaseous oxidized mercury, and particulate-bound mercury. GEM, the dominant form of atmospheric mercury, is ubiquitous in the atmospheric reservoir and originates from a multitude of anthropogenic and natural sources (Edwards et al., 2021; Gaffney and Marley, 2014; Gustin et al., 2020; Gworek et al., 2020). Near the surface (marine or terrestrial boundary layer) and outside polar regions, gaseous oxidized mercury and particulate-bound mercury represent only a few percent of the total atmospheric mercury (Gustin and Jaffe, 2010; Gustin et al., 2015; Swartzendruber et al., 2006). Chemical cycling and the spatiotemporal distribution of mercury in the air are still poorly understood regardless of the atmospheric layer considered (surface, mixed or free troposphere, stratosphere), and complete GEM oxidation schemes remain unclear (Shah et al., 2021, and associated references). Still, several studies provided evidence that the vertical distribution of atmospheric mercury measurements from the boundary layer to the lower or upper troposphere and stratosphere shows a decreasing trend in GEM concentration with increasing altitude, in parallel with an increase in the concentration of divalent mercury resulting from GEM oxidation mechanisms

(Brooks et al., 2014; Faïn et al., 2009; Fu et al., 2016; Koenig et al., 2023; Lyman and Jaffe, 2012; Murphy et al., 2006; Swartzendruber et al., 2006, 2008; Sheu et al., 2010; Talbot et al., 2007). The identification of such observational processes (lower concentration of GEM in high-altitude air masses compared to those in the marine boundary layer ones) is used here to help characterize possible intrusions of high-altitude air masses at the low-altitude Pointe Benedicte observatory.

2.3 Water vapor isotopic measurements

The near-surface water vapor $\delta^{18}\text{O}$ and δD (hereafter $\delta^{18}\text{O}_v$ and δD_v , ‰, vs. SMOW and enabling us to calculate water vapor d-excess_v as $\text{d-excess}_v = \delta\text{D}_v - 8 \times \delta^{18}\text{O}_v$). The water vapor mixing ratio (q_v , ppmv) has been measured continuously since November 2019. The measurements have been made with a Picarro Inc. instrument (L2130-i model) based on wavelength-scanned cavity ring-down spectroscopy. The instrument is installed in a temperature-controlled room at the Amsterdam Island observatory, and the sampling of water vapor is done outside at $\sim 6 \text{ m}$ above ground level (or 76 m above sea level) through a 5 m long inlet tube made of PFA (perfluoroalkoxy alkanes) and heated at 40°C .

The calibration of the water vapor mixing ratio was performed in the laboratory before sending the instrument to Amsterdam Island. In the field, we found excellent agreement between the mixing ratio measured by the Picarro instrument and the mixing ratio measured by the weather station (the difference between the two records always stays below 2 ‰, and there is no systematic shift between the two records).

The calibration of the water isotopic data is performed in several steps following previous studies (Leroy-Dos Santos et al., 2020; Tremoy et al., 2011) and using a standard delivery module by Picarro. First, we quantified the influence of the water vapor mixing ratio on the water isotope ratios. This effect is large at very low humidity (Leroy-Dos Santos et al., 2021). It can also depend on the isotopic composition of the standard water (Weng et al., 2020). Here, we introduced two different water standards, EPB-AMS and GREEN-AMS, with respective values of (-5.66 ‰ , -47.31 ‰) and (-32.65 ‰ , -263.76 ‰) for the couple ($\delta^{18}\text{O}$, δD) which encompass the isotopic values observed on site. While we would expect a constant null value for $(\delta^{18}\text{O}_{\text{measured}} - \delta^{18}\text{O}_{\text{standard}})$ in Fig. 2 because we always inject the same water standards, the measured $\delta^{18}\text{O}$ values of both the EPB-AMS and GREEN-AMS standards in fact decrease with increasing humidity at the same amplitude. The $(\delta\text{D}_{\text{measured}} - \delta\text{D}_{\text{standard}})$ displayed in Fig. 2 also shows variations, but in contrast to the relative evolution of $\delta^{18}\text{O}$ with respect to the water vapor mixing ratio, the δD measurements of the EPB-AMS and GREEN-AMS standards exhibit different behavior: the δD of EPB-AMS increases by 1.5 ‰, and

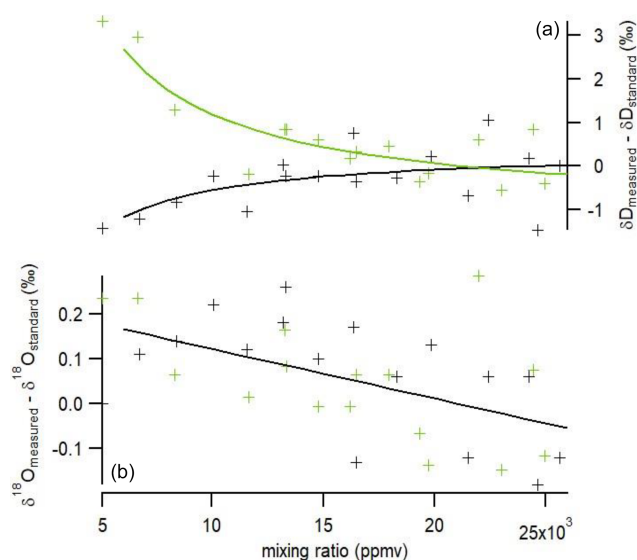


Figure 2. Influence of the water vapor mixing ratio on measured δD (a) and $\delta^{18}O$ (b) (anomaly from the true value of the standard). The results are shown for two different standards (GREEN_AMS in green and EPB_AMS in black). The crosses indicate the data obtained with the setup, and the solid lines are the best regression curves (same curve for $\delta^{18}O$ for both standards).

the δD of GREEN-AMS decreases by 2.5‰ over the same 6000–24 000 ppmv range for the water vapor mixing ratio q_v .

As a consequence, the raw $\delta^{18}O_v$ measurements are corrected with the following regression:

$$\delta^{18}O_{v,\text{corr}} = \delta^{18}O_{v,\text{measured}} + 1.1 \cdot 10^{-5} \times q + 0.232. \quad (4)$$

For the correction of the raw δD_v , we use two different regression splines for EPB-AMS and GREEN-AMS (see Fig. 2):

$$\delta D_{\text{EPB-AMS,corr}} = \delta D_{\text{EPB-AMS,measured}} + \frac{9300}{q} - 0.383, \quad (5)$$

$$\delta D_{\text{GREEN-AMS,corr}} = \delta D_{\text{GREEN-AMS,measured}} - \frac{22400}{q} + 1.05. \quad (6)$$

The raw δD_v are thus weighted-corrected according to their distance to the EPB_AMS and GREEN_AMS splines as follows:

$$\begin{aligned} \delta D_{v,\text{corr}} = & \delta D_{\text{GREEN-AMS,corr}} \\ & + \frac{\delta D_{v,\text{measured}} - \delta D_{\text{GREEN-AMS,measured}}}{\delta D_{\text{EPB-AMS,measured}} - \delta D_{\text{GREEN-AMS,measured}}} \\ & \times (\delta D_{\text{EPB-AMS,corr}} - \delta D_{\text{GREEN-AMS,corr}}). \end{aligned} \quad (7)$$

This first calibration step (correction from the influence of the mixing ratio on the isotopic composition) has been performed every year over the whole range of mixing ratio values and provided very similar results from one year to the other. The second calibration step consists of the injection of the same two isotopic standards every 47 h at a water

vapor mixing ratio of 13 000 ppmv to correct for any long-term drift. The correction associated with this drift is less than 0.4‰ for $\delta^{18}O$ and 2.5‰ for δD over the 2 years of measurements.

Precipitation was also sampled on a weekly basis in a rain gauge filled with paraffin oil, which permits us to have measurements of water isotopic composition in the precipitation on a weekly basis. The water samples are then sent for analyses to the LSCE (Laboratoire des Sciences du Climat et de l'Environnement) and measured with an L2130-i isotopic analyzer by Picarro. The uncertainty associated with this series of measurements is ± 0.15 ‰ for $\delta^{18}O$ and ± 0.7 ‰ for δD , leading to an uncertainty of ± 1.4 ‰ for d-excess.

2.4 Back trajectories: FLEXPART

The origin and trajectory of air masses were calculated by FLEXPART, which is a Lagrangian particle dispersion model (Pisso et al., 2019). All the meteorological data used to simulate the back trajectories are taken from the ERA5 atmospheric reanalysis (Hersbach et al., 2020) with a 6-hourly resolution. The ERA5 reanalysis is carried out by the European Centre for Medium-Range Weather Forecasts (ECMWF) using its Earth system model IFS (Integrated Forecasting System), cycle 41r2. For a few selected events, we used FLEXPART to calculate back trajectories over 5 d with 1000 launches of neutral particles (sensitivity test) of inert air tracers released randomly (volume of $0.1^\circ \times 0.1^\circ \times 100$ m) every 3 h at 100 m above sea level (Leroy-Dos Santos et al., 2020) centered around the coordinates of Amsterdam Island. The results of the FLEXPART back trajectories are then displayed as particle probability density as well as through the location of their humidity-weighted averages.

2.5 General atmospheric circulation model equipped with water stable isotopes

2.5.1 LMDZ-iso model (Laboratoire de Météorologie Dynamique Zoom model equipped with water isotopes)

LMDZ-iso (Risi et al., 2010) is the isotopic version of the atmospheric general circulation model LMDZ6 (Hourdin et al., 2020). We have used LMDZ-iso version 20230111.trunk with the physical package NPv6.1, identical to the atmospheric setup of IPSL-CM6A (Boucher et al., 2020) used for phase 6 of the Coupled Model Intercomparison Project (CMIP6, Eyring et al., 2016). We performed two simulations, one at very low horizontal resolution (VLR, 3.75° in longitude and 1.9° in latitude, 96×95 grid cells) and the second at low horizontal resolution (LR, 2.0° in longitude and 1.67° in latitude, 144×142 grid cells). Both simulations have 79 vertical levels, and the first atmospheric level is located around 10 m above ground level. The LMDZ-iso 3D fields of temperature and wind are nudged toward the 6-hourly ERA5 reanalysis data with a relaxation time of 3 h. Surface ocean

boundary conditions are taken from the monthly mean sea surface temperature (SST) and sea ice fields from the CMIP6 AMIP Sea Surface Temperature and Sea Ice dataset version 1.1.8 (Durack et al., 2022; Taylor et al., 2000). LMDZ-iso outputs are used at a 3-hourly resolution. Amsterdam Island (58 km²) is too small to be represented in the LMDZ-iso model.

2.5.2 ECHAM6-wiso model (European Centre Hamburg model equipped with water isotopes)

ECHAM6-wiso (Cauquoin et al., 2019; Cauquoin and Werner, 2021) is the isotopic version of the atmospheric general circulation model ECHAM6 (Stevens et al., 2013). The implementation of the water isotopes in ECHAM6 has been described in detail by Cauquoin et al. (2019) and has been updated in several aspects by Cauquoin and Werner (2021) to make the model results more consistent with the last findings based on water isotope observations (isotopic composition of snow on sea ice considered, supersaturation equation slightly updated, and kinetic fractionation factors for oceanic evaporation assumed to be independent of wind speed). We have used ECHAM6-wiso model outputs from a simulation with a T127L95 spatial resolution (0.9° horizontal resolution and 95 vertical levels). ECHAM6-wiso is thus run with a finer resolution than both LMDZ-iso simulations. The ECHAM6-wiso 3D fields of temperature, vorticity, and divergence as well as the surface pressure field were nudged toward the ERA5 reanalysis data every 6 h (Hersbach et al., 2020). The orbital parameters and greenhouse gas concentrations have been set to the values of the corresponding model year. The monthly mean sea surface temperature and sea ice fields from the ERA5 reanalysis have been applied as ocean surface boundary conditions as well as a mean $\delta^{18}\text{O}$ of surface seawater reconstruction from the global gridded dataset of LeGrande and Schmidt (2006). As no equivalent dataset of the δD composition of seawater exists, the δD of the seawater in any grid cell has been set equal to the related $\delta^{18}\text{O}$ composition, multiplied by a factor of 8, in accordance with the observed relation for meteoric water on a global scale (Craig, 1961). The ECHAM6-wiso simulation is described in detail and evaluated by Cauquoin and Werner (2021). ECHAM6-wiso outputs are given at a 6-hourly resolution. As for the LMDZ-iso model, Amsterdam Island (58 km²) is too small to be represented by ECHAM6-wiso.

3 Results

3.1 Data description

3.1.1 Temporal variability in the meteorological records

As mentioned earlier, there is a clear annual cycle at Amsterdam Island, as recorded in the temperature and water vapor mixing ratio for the years 2020 and 2021. The December–February period (austral summer) has the highest temper-

atures with an average of 15.0 °C, while in winter (July–September) the average temperature varies around 10.5 °C. In parallel, we do not see clear patterns of a diurnal cycle in the temperature record, except for some periods with a small amplitude (4–5 °C).

The impact of synoptic events at the scale of a few days is visible in the temperature and water mixing ratio with a covariation of the temperature and water vapor mixing ratio and amplitudes of up to 10 °C and more than 10 000 ppmv.

3.1.2 Temporal variability in the GEM record

Previous studies clearly showed that AMS is little influenced by anthropogenic sources of mercury and greatly influenced by the ocean surrounding the island (Angot et al., 2014; Hoang et al., 2023; Jiskra et al., 2018; Li et al., 2023; Slemr et al., 2015, 2020). Angot et al. (2014) reported mean annual GEM concentrations of about $1.03 \pm 0.08 \text{ ng m}^{-3}$ from 2012 to 2013. These concentrations are $\sim 30\%$ lower than those measured at remote sites of the Northern Hemisphere. Over the period 2012 to 2017, Slemr et al. (2020) confirmed that higher GEM concentrations can be found during austral winter. Lower GEM values are generally observed in October and November as well as in January and February during austral summer. Using this 6-year long dataset, the mean annual GEM concentration is $1.04 \pm 0.07 \text{ ng m}^{-3}$ (annual range 1.014 to 1.080 ng m^{-3}), i.e., very close to the one observed by Angot et al. (2014).

Surprisingly, unlike the 2012–2017 dataset, the GEM presented in this study did not show a significantly higher mean concentration during the austral winter months than during the summer months (Fig. 3), with consequently no discernible seasonal amplitude of GEM. On a finer timescale, the lack of a clear pattern of the GEM seasonal cycle is counterbalanced by days showing abrupt increases or decreases in concentrations. Some of the sudden GEM decreases appear concomitant with important negative peaks of several per mille in $\delta^{18}\text{O}_v$.

3.1.3 Temporal variability of water isotopic composition

The isotopic composition of precipitation ($\delta^{18}\text{O}_p$) sampled on a weekly basis displays a quite large variability ($\delta^{18}\text{O}_p = -3.06 \pm 1.75\text{‰}$, $n = 104$) with values slightly higher during austral summer (the difference between summer and winter $\delta^{18}\text{O}_p$ values is about 2‰ to 3‰) (Fig. 3). No significant seasonal variations are observed in the record of d-excess of precipitation (not shown).

No diurnal cycle can be detected in the $\delta^{18}\text{O}_v$ and d-excess_v. An annual cycle is not visible either (1‰ difference between the summer and winter mean $\delta^{18}\text{O}_v$ values, while the standard deviation of the entire record at 1 h resolution is 1.7‰). Only the synoptic-scale variability is well expressed in the records of $\delta^{18}\text{O}_v$ and d-excess_v with an anticorrelation between both parameters when looking at the 2-year series at

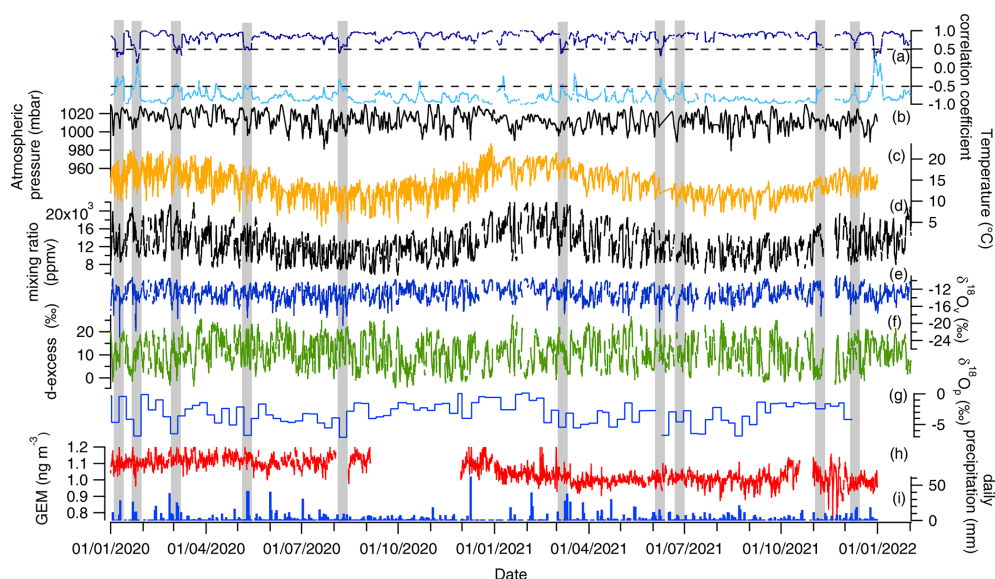


Figure 3. Meteorological, isotopic, and GEM records for the years 2020 and 2021 on the Amsterdam Island (a) correlation coefficient between $\delta^{18}\text{O}_v$ and the mixing ratio (dark blue, top) and between $\delta^{18}\text{O}_v$ and d-excess $_v$ (light blue, bottom) over a moving time window of 8 d, (b) atmospheric pressure (hourly average), (c) atmospheric temperature (hourly average), (d) water vapor mixing ratio (hourly average), (e) $\delta^{18}\text{O}_v$ (hourly average), (f) d-excess $_v$ (hourly average), (g) $\delta^{18}\text{O}$ of precipitation sampled on a weekly basis, (h) GEM concentration (hourly average), and (i) daily precipitation. The grey-shaded areas indicate the negative excursions in $\delta^{18}\text{O}_v$ associated with decorrelation between the water vapor mixing ratio and $\delta^{18}\text{O}_v$ and a correlation coefficient > -0.5 between d-excess $_v$ and $\delta^{18}\text{O}_v$.

hourly resolution ($R^2 = 0.61$, with R^2 being the coefficient of determination for a linear regression). Moreover, $\delta^{18}\text{O}_v$ is correlated most of the time with the water vapor mixing ratio ($R^2 = 0.55$ for the 2-year series at hourly resolution).

There are a few exceptions to the general correlation between the water vapor $\delta^{18}\text{O}$ and the water vapor mixing ratio as illustrated in Fig. 3. Short periods of a few days are associated with a decrease in the correlation coefficient R estimated from the correlation between $\delta^{18}\text{O}_v$ and q_v (R is calculated continuously from hourly records on an 8 d moving window). The periods of low R are also often characterized by a negative peak of several per mille in $\delta^{18}\text{O}_v$, which is not visible in the d-excess $_v$. During these $\delta^{18}\text{O}_v$ excursions, the general anticorrelation between $\delta^{18}\text{O}_v$ and d-excess $_v$ hence also breaks down. Our study mostly focuses on the 11 most prominent abrupt events highlighted in the $\delta^{18}\text{O}_v$ record (only 10 visible in Fig. 3 because of the scale). The 11 most abrupt events occurring when the correlation coefficient R between $\delta^{18}\text{O}_v$ and d-excess $_v$ is larger than -0.5 are associated with a $\delta^{18}\text{O}_v$ negative excursion larger than 3‰ (at 6 h resolution) over a period of less than 24 h, the length of the event being measured between the middle slopes of the decrease and a subsequent increase in the $\delta^{18}\text{O}_v$. The 11 selected negative excursions occur at a rate larger than -0.5‰ h^{-1} , and the $\delta^{18}\text{O}_v$ increase at the end of each excursion has an amplitude larger than half the amplitude of the corresponding initial decrease.

3.2 Model–data comparison

We selected a 3-month period (January to March 2020) for the comparison between our dataset and the outputs of the ECHAM6-wiso and LMDZ-iso models. This period has been selected for display because it encompasses 4 out of the 11 negative excursions of $\delta^{18}\text{O}_v$, but the extended comparison over the whole 2-year period is displayed in Fig. A1. There is overall agreement between the measured and modeled $\delta^{18}\text{O}_v$ and water vapor mixing ratio (Fig. 4). The best agreement over the 3-month series is obtained with the ECHAM6-wiso and LMDZ-iso (LR) models ($R^2 = 0.59\text{--}0.6$ and $0.87\text{--}0.90$, respectively, for $\delta^{18}\text{O}_v$ and water vapor mixing ratio series), while slightly less good agreement is observed with the VLR simulation of the LMDZ-iso model ($R^2 = 0.49$ and 0.79 , respectively, for $\delta^{18}\text{O}_v$ and the water vapor mixing ratio series). The same observation can be made of the entire 2-year time series. We also compare the precipitation amount modeled by ECHAM6-wiso and LMDZ-iso to the precipitation amount measured by the Météo-France weather station. The correlation between modeled and measured precipitation is close to zero for LMDZ-iso ($R^2 = 0.08\text{--}0.13$ for VLR–LR), while there is better agreement when comparing the measured precipitation amount to outputs of ECHAM6-wiso ($R^2 = 0.45$). Finally, when focusing on the short-term negative $\delta^{18}\text{O}_v$ excursions (Figs. 4 and A1), they are in general more strongly expressed in the measurement time series than in the model series. Part of this disagreement can be explained by the fact that the $\delta^{18}\text{O}_v$ record has a higher tem-

poral resolution (1 h) than the model outputs (3 h for LMDZ-iso and 6 h for ECHAM6-wiso). However, when interpolating the $\delta^{18}\text{O}_v$ record at a 6 h resolution (dotted dark blue), the negative excursions are still clearly visible but not captured by the LMDZ-iso model (Fig. 4 and Table 1). When looking at the whole 2-year series, the LMDZ-iso VLR simulation fails to reproduce most of these $\delta^{18}\text{O}_v$ excursions (only the negative excursion of 3 January 2020 is reproduced), while the ECHAM6-wiso model is able to capture all the $\delta^{18}\text{O}_v$ excursions. The LMDZ-iso LR simulation produces a negative $\delta^{18}\text{O}_v$ excursion over many events with a significantly lower amplitude than in the data and in the ECHAM6-wiso model (Table 1).

4 Discussion

The most remarkable pattern from this 2-year series is the succession of short negative excursions of $\delta^{18}\text{O}_v$ associated with decorrelation between $\delta^{18}\text{O}_v$ and humidity, $\delta^{18}\text{O}_v$, and $d\text{-excess}_v$ and which is highlighted with grey-shaded areas in Fig. 3, as detailed in Figs. 5 and A2 and referenced in Table 1. These negative $\delta^{18}\text{O}_v$ excursions always occurred during low-pressure periods (atmospheric pressure below 1005 mbar), and we observe the presence of a cold front within a distance of 100 km around Amsterdam Island in a 48 h period covering the time of the event (Supplement Fig. S1). The focus on the first 3 months of the series presented in Fig. 4 shows that these events are captured by ECHAM6-wiso at 0.9° resolution but not systematically by LMDZ-iso at $2 \times 1.67^\circ$ and even less so by LMDZ-iso at $3.75 \times 1.9^\circ$ resolution. Such a mismatch makes the understanding of the processes at play during these events particularly important to investigate to further improve the performances of atmospheric general circulation models equipped with water isotopes.

Several hypotheses can be proposed to explain the negative excursions of $\delta^{18}\text{O}_v$. The beginning of these excursions is associated with a decrease in the water vapor mixing ratio and occurs in most cases during a precipitation event (Table 1). These events share similarities with negative $\delta^{18}\text{O}_v$ and $\delta^{18}\text{O}_p$ short events previously observed in temperate regions during a cold front passage (e.g., Aemisegger et al., 2015). Three possible processes at play to explain such events have already been listed in previous studies (e.g., Dütsch et al., 2016): (i) local interaction between the vapor and the rain droplets (rain equilibration and rain evaporation), (ii) vertical subsidence of water vapor with depleted isotopic composition, or (iii) horizontal advection through the arrival of a cold front. We explore below how we can gain information on the different processes using our dataset, back trajectories, and model–data comparison.

Table 1. List of the 11 events associated with loss of correlation between $\delta^{18}\text{O}_v$ and q_v , $\delta^{18}\text{O}_v$ and $d\text{-excess}_v$, and negative excursions of $\delta^{18}\text{O}_v$ over 2020–2021. The amplitude of the negative $\delta^{18}\text{O}_v$ anomaly is calculated from the minimum of $\delta^{18}\text{O}_v$ on the record at hourly resolution (at 6 h resolution). When the calculated amplitude is smaller than 1‰, we indicate only “–”. When the vertical velocity is between -0.25 and 0.25 Pa s^{-1} , this is indicated in the table as “ ~ 0 ”.

Date of the event (dd/mm/yyyy)	Negative excursion of GEM	Low pressure (< 1005 mbar)	Rain	Relative humidity at the surface (at minimum 18O_v)	Vertical velocity from reanalyses (850 hPa)	Vertical velocity from reanalyses (500 hPa)	Length of the event (h)	Amplitude of the $\delta^{18}\text{O}_v$ peak in the data (‰)	Amplitude of the $\delta^{18}\text{O}_v$ peak in ECHAM-wiso (‰)	Amplitude of the $\delta^{18}\text{O}_v$ peak in LMDZ-iso VLR (‰)	Amplitude of the $\delta^{18}\text{O}_v$ peak in LMDZ-iso LR (‰)
06/12/2021	Yes	Yes	Yes	82%	~ 0	Up	3 h	-6 (-5)	-2.3	-	-2
08/11/2021	Yes	Yes	No	85%	~ 0	~ 0	17 h	-5.5 (-5.5)	-5	-	-4
23/06/2021	No	Yes	Yes	75%	~ 0	~ 0	10 h	-5.5 (-5.4)	-6	-	-
07/06/2021	No	Yes	Yes	80%	Up	~ 0	9 h	-6.5 (-5.8)	-5.8	-	-2
08/03/2021	Yes	Yes	Yes	89%	Down	Up	20 h	-6 (-6)	-4	-	-
09/08/2020	No data	Yes	Yes	87%	Down	Up	8 h	-8 (-6)	-7	-	-2
10/05/2020	Small	Yes	Yes	95%	Down	Down	14 h	-4.9 (-4)	-3	-	-3
04/03/2020	No data	Yes	Yes	98%	Up	Up	9 h	-6.1 (-5.3)	-5	-	-
24/01/2020 (double peak)	Yes	Yes	Yes	93% and 90%	1st peak up and 2nd peak down	1st peak up and 2nd peak down	17 h	-7.8 (-7.5)	-4.5	-	-3.5
09/01/2020	Yes	Yes	Yes	94%	Up	Up	4 h	-9 (-4)	-5	-	-
03/01/2020	Yes	Yes	No	90%	Down	~ 0	6 h	-2.8 (-2.5)	-2.4	-3	-3.5

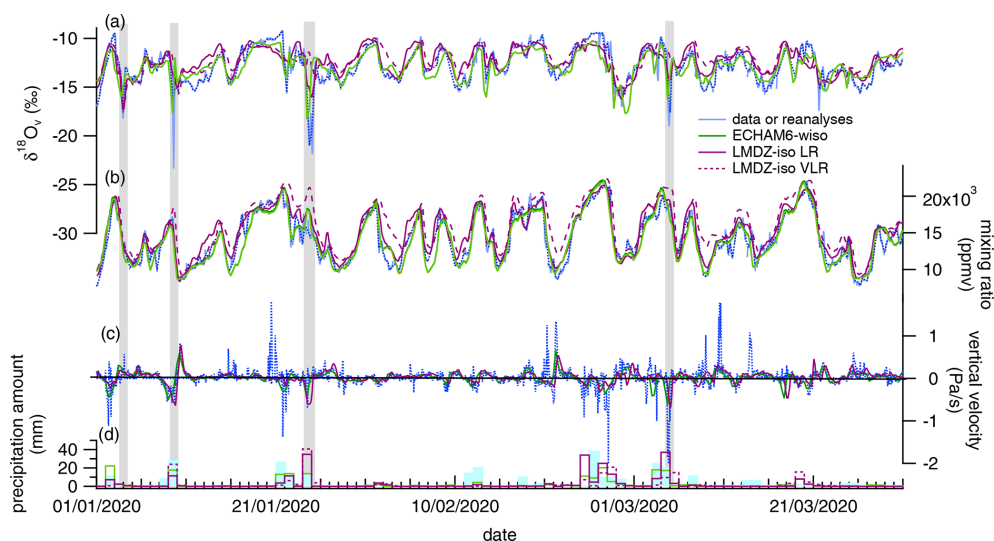


Figure 4. Model–measurement comparison (January–March 2020): (a) $\delta^{18}\text{O}_v$ (light blue for data on hourly average, dotted dark blue for data resampled at a 6 h resolution); (b) water vapor mixing ratio from our dataset; (c) vertical velocity; (d) precipitation amount. The grey-shaded areas highlight the negative $\delta^{18}\text{O}_v$ excursions as defined in Sect. 3.1.3 (note that in this figure the excursions of 3 and 9 January 2020 are distinct, while the distinction could not be made in Fig. 3 because of the scale).

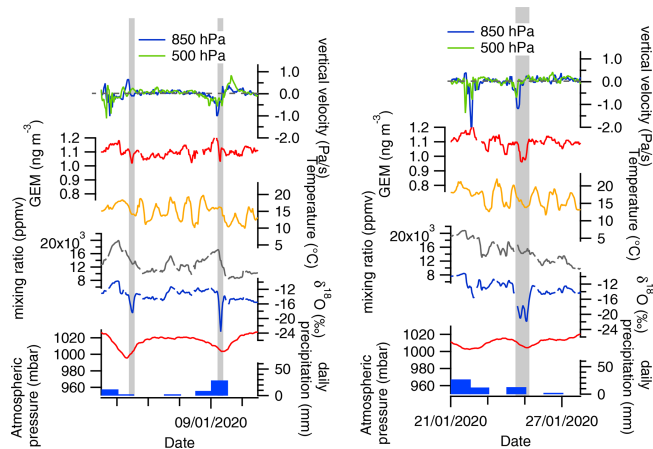


Figure 5. Evolution of the GEM, $\delta^{18}\text{O}_v$, water vapor mixing ratio, and meteorological parameters (surface temperature, surface atmospheric pressure, daily precipitation) measured by the Météo-France weather station and vertical velocity from the ERA5 reanalyses at 500 and 850 hPa over the three isotopic excursions of January 2020 (a, b) identified in Fig. 4. A focus on the other excursions is provided in Fig. A2.

4.1 $\delta^{18}\text{O}_v$ – q_v relationship

First, to test the hypothesis of vapor–droplet interactions, we looked at the $\delta^{18}\text{O}_v$ vs. q_v distribution following the approach already used by Guilpart et al. (2017) (Fig. 6). We acknowledge that our approach is crude and should be taken as a first-order approach since we can only look at the water vapor $\delta^{18}\text{O}_v$ vs. q_v distribution in the surface layer using adapted boundary conditions, while it may be more relevant

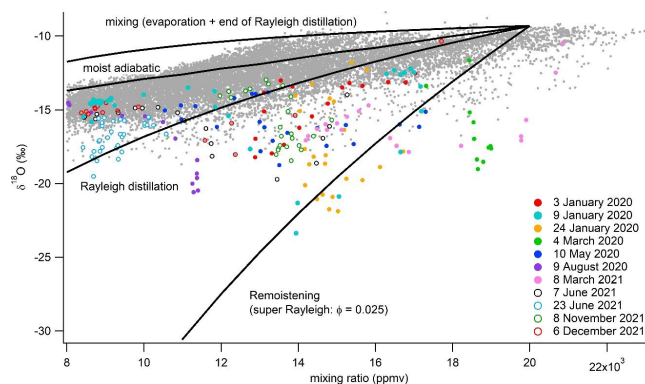


Figure 6. Relative evolution of q_v and $\delta^{18}\text{O}_v$ for the different events (colors according to the date as explained in the graph) and for the entire 2-year records (grey). The solid lines are theoretical lines whose equations are detailed in Noone (2012) for different processes (re-moistening associated with exchange between rain and water vapor; Rayleigh distillation assuming that all formed condensation is removed from the cloud; a moist adiabatic process assuming that liquid condensation stays in the cloud with the water vapor; mixing of water vapor from ocean evaporation around Amsterdam Island and water vapor from the end of the Rayleigh distillation, i.e., high-altitude water vapor). The water vapor for the calculation of Rayleigh distillation and for the evaporation above the ocean has a $q_{v,0}$ of 20 000 ppmv and a $\delta^{18}\text{O}_{v,0}$ of -9.3‰ . The vapor at the end of the distillation line has a water vapor mixing ratio of 1000 ppmv and a $\delta^{18}\text{O}_v$ of -40‰ .

to look at this relationship in the free troposphere. In general, the $\delta^{18}\text{O}_v$ vs. q_v evolution lies on a curve which can be explained by condensation processes (Rayleigh distilla-

tion or reversible moist adiabatic process). However, for the 11 events highlighted above, the water vapor $\delta^{18}\text{O}_v$ vs. q_v evolution follows an evolution standing below the curve of the $\delta^{18}\text{O}_v$ vs. q_v evolution observed for the rest of the series. Although the evolution of the water vapor $\delta^{18}\text{O}_v$ vs. q_v is rather abrupt, there is a certain resemblance to the idealized theoretical re-moistening curve initially calculated for the free troposphere (Noone, 2012) and adapted here with initial conditions corresponding to the isotopic composition of surface water vapor. Re-moistening is described through a modification of the equilibrium fractionation coefficient between water vapor and rain (α_e), so that the effective fractionation factor is $\alpha = (1 + \varphi) \times \alpha_e$, φ being the degree to which α deviates from equilibrium. This effective fractionation coefficient is then introduced in the Rayleigh distillation equation to deduce the link between $\delta^{18}\text{O}_v$ and the mixing ratio as

$$\delta^{18}\text{O}_v - \delta^{18}\text{O}_{v,0} = (\alpha - 1) \times \ln(q_v/q_{v,0}). \quad (8)$$

Despite the simplicity of our approach, the fact that the water vapor $\delta^{18}\text{O}_v$ vs. q_v evolution lies below the idealized curve for condensation processes supports the depleting effect of vapor–rain interactions for our negative water vapor $\delta^{18}\text{O}_v$ excursions (Noone, 2012; Worden et al., 2007). Surface relative humidity remains relatively high during these events (values given in Table 1 compared to a mean value of 77 %), which favors rain–vapor diffusive exchanges. This interpretation is also supported by the stable d-excess_v during these events.

4.2 $\delta^{18}\text{O}_v$ –GEM relationship

Second, to test the hypothesis of subsidence of air from higher altitudes, GEM is used. Indeed, aircraft measurements and model simulations demonstrated that the upper troposphere or lower stratosphere is depleted in GEM and enriched in species composed of reactive gaseous mercury and particulate-bound mercury (Lyman and Jaffe, 2012; Murphy et al., 2006; Sillman et al., 2007; Swartzendruber et al., 2006, 2008; Talbot et al., 2007, 2008). This leads to lower GEM concentrations than those usually observed when the lowest atmosphere layer is only under marine influence (Angot et al., 2014; Lindberg et al., 2007). The fact that GEM negative excursions are observed in phase with negative $\delta^{18}\text{O}_v$ excursions in most of the events (six events out of a total of nine events with GEM data; see Figs. 5 and A2 as well as Table 1) suggests that vertical subsidence of water vapor, $\delta^{18}\text{O}$ -depleted by Rayleigh distillation and/or rain–vapor interactions, can have an influence on the observed excursions of $\delta^{18}\text{O}_v$, in agreement with the conclusion of Dütsch et al. (2016).

4.3 Back-trajectory information

To further explore the processes leading to the decoupling of humidity and $\delta^{18}\text{O}_v$ as well as sharp negative excursions of $\delta^{18}\text{O}_v$ during the 11 events identified here, we also use information from the ERA5 reanalyses. In particular, the influence of atmospheric circulation (vertical and horizontal advection) and moisture origin can be studied through back trajectories. The back trajectories, presented here for three events (Figs. 7, A3, and A4), confirm the information from wind directions that there is no systematic change in the horizontal origin of the trajectories for the different events. No systematic pattern is identified either in the vertical advection even if we note that, for the event of 3 January, the average altitude of the envelope of the 5 d back trajectories increases when comparing the situation before the excursion and the situation when the most negative $\delta^{18}\text{O}_v$ values are reached. This observation may support the occurrence of air subsidence, as indicated by the GEM record for this particular event (Fig. 5).

The subsidence over the different events can better be studied from the vertical velocity from the ERA5 reanalyses (Figs. 4 and A1). Subsidence (positive vertical velocity) is not systematically associated with negative $\delta^{18}\text{O}_v$ excursions: subsidence at either 850 or 500 hPa is observed for only 5 events of 11 (Table 1). In four cases, there is rather an ascending movement of the atmospheric air associated with the rain event. In the other cases, there is no clear vertical movement. However, we note that, when negative $\delta^{18}\text{O}_v$ excursions are not concomitant with subsidence, they occur at the end of an ascending movement which is generally followed by subsidence (Figs. A1 and A2).

4.4 Model–data comparison and atmospheric dynamics

With the information gathered above, both subsidence and isotopic depletion associated with rain occurrence and further interaction between droplets and water vapor can explain the negative excursions of $\delta^{18}\text{O}_v$. We note however that the data gathered so far do not permit us to provide a simple and unique explanation. Neither subsidence nor rain systematically occurred for each of the $\delta^{18}\text{O}_v$ excursions. Still, the fact that at least ECHAM6-wiso is able to reproduce every negative $\delta^{18}\text{O}_v$ excursion (whether they are associated or not with subsidence or rainwater vapor re-equilibration) shows that (1) the patterns of the atmospheric water cycle are correctly reproduced, a validation which can be performed using humidity and precipitation data for some aspects while benefiting from water isotope implementation for the residence time of water; and (2) the isotopic processes are correctly implemented in this model. Such abrupt $\delta^{18}\text{O}_v$ events can hence be used as a test bed of the performances of water-isotope-enabled general circulation models.

To further explore the $\delta^{18}\text{O}_v$ data–model comparison and the associated processes, we compare the performances of the ECHAM6-wiso and LMDZ-iso models over the first

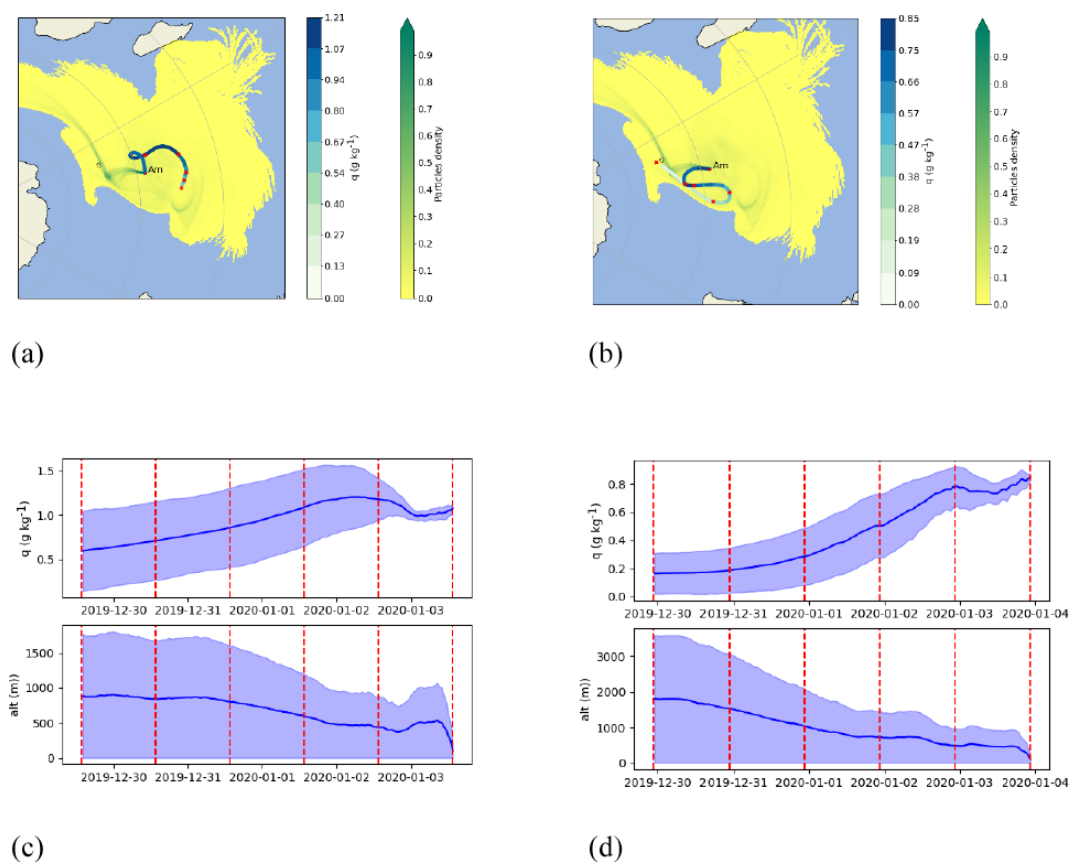


Figure 7. FLEXPART footprints of 5 d back trajectories for the event of 3–4 January. **(a)** Latitude–longitude projection of the FLEXPART back-trajectory footprints for 3 January 2020 at 13:30. The yellow to green colors at each grid point of these projections represent the density of particles. The white to blue colors indicate the water vapor mixing ratio along the humidity-weighted average back trajectory. Each red point indicates the location of the average back trajectory for each of the 5 d before the date of the considered event. **(b)** Same as for 3 January 2020 at 22:30. **(c)** The top shows the evolution of the water vapor mixing ratio of the back trajectories for 3 January 2020 at 13:30; the bottom shows the altitude evolution of the back trajectory for 3 January 2020 at 13:30. **(d)** Same as panel (c) for 3 January 2020 at 22:30.

months of 2020 in terms of atmospheric dynamics (Figs. 4 and A1). First, and as expected because of the nudging, the two models reproduce rather well the evolution of the vertical velocity of the ERA5 reanalyses, with a stronger ascent for the model predicting the strongest precipitation amount (e.g., LMDZ-iso for 24 January 2020). The event of 3 January is the only one reproduced by both ECHAM6-wiso and the two versions of the LMDZ-iso model: the three simulations show a clear subsidence over the isotopic event and a clear negative $\delta^{18}\text{O}_v$ excursion. For the other events, neither LMDZ-iso nor ECHAM6-wiso shows a clear signal of subsidence at 500 or 850 hPa (not shown). However, the horizontal distributions of vertical velocity obtained with ECHAM6-wiso and LMDZ-iso are significantly different (Fig. 8 for the event of 9 January, Figs. S2 and S3 for the other events). While the LMDZ-iso-modeled vertical velocity displays a rather strong homogeneity on the vertical axis, the ECHAM6-wiso-modeled vertical velocity highlights subsidence of air below the ascending column, with the maximum of the negative $\delta^{18}\text{O}_v$

anomaly at the surface located just at the limit between ascendance and subsidence (between 75 and 77° E in Fig. 8c). This subsidence of depleted $\delta^{18}\text{O}_v$ below the ascending column is responsible for the sharp negative $\delta^{18}\text{O}_v$ excursion in the ECHAM6-wiso model. The fact that subsidence of air occurs just below uplifted air, at the limit between ascendance and subsidence (Figs. 8k and S2), permits us to reconcile the GEM data, suggesting subsidence, and the sign of the vertical velocity of the ERA5 reanalyses at Amsterdam Island suggests that many excursions start with ascendance. Since the isotope implementation was done similarly in the two models, the reason why the LMDZ-iso model does not reproduce the water isotopic anomaly is its too coarse resolution, as also supported by the comparison between performances of the LMDZ-iso model at low resolution and very low resolution for the event of 24 January (Table 1 and Fig. 4). As already pointed out by Ryan et al. (2000), a fine resolution is necessary for correctly simulating front dynamics, and we

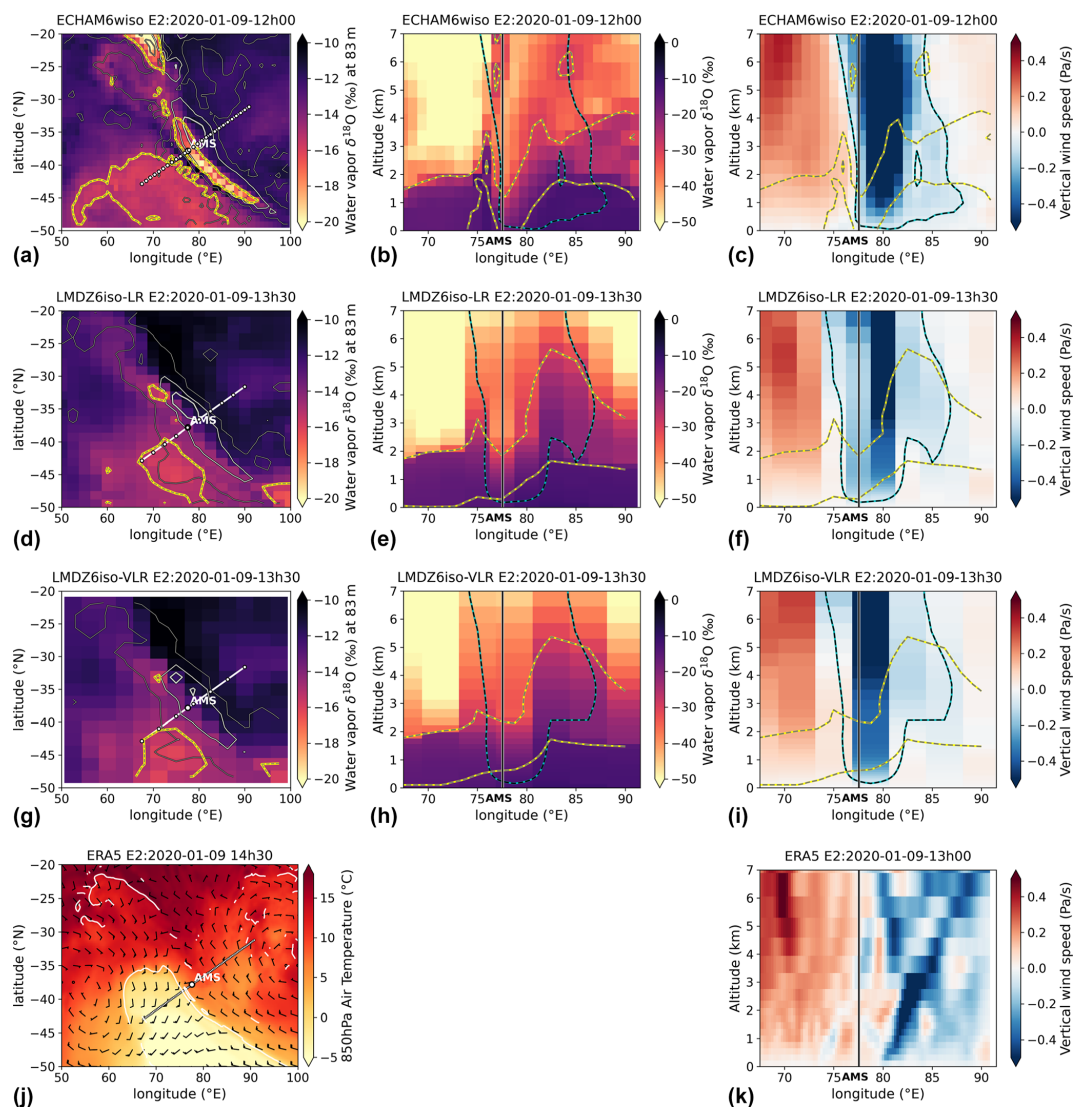


Figure 8. Modeled $\delta^{18}\text{O}_v$ and vertical velocity for the event of 9 January 2020. **(a)** Surface air $\delta^{18}\text{O}_v$ (~ 83 m, latitude vs. longitude), with yellow lines indicating the -15‰ contour level and grey lines indicating precipitation contours at 0.5, 10, and 50 mm d^{-1} (thin, medium, and thick lines, respectively). **(b)** $\delta^{18}\text{O}_v$ plotted on a vertical cross section (altitude vs. longitude) along the transect indicated by the white line in panel **(a)**, with yellow lines indicating $\delta^{18}\text{O}_v$ contours at -30‰ and -15‰ , blue lines indicating the contour of -0.05 Pa s^{-1} vertical velocity (ascendancy), and the vertical black line denoting the longitude of Amsterdam Island. **(c)** Vertical velocity plotted on a vertical cross section as for panel **(b)** with the same contour lines. Panels **(a)**, **(b)**, and **(c)** are drawn using outputs of the ECHAM6-wiso model. Panels **(d)**, **(e)**, and **(f)** are the same as panels **(a)**, **(b)**, and **(c)** but obtained from the LMDZ-iso model at low resolution (LR). Panels **(g)**, **(h)**, and **(i)** are the same as panels **(a)**, **(b)**, and **(c)** but obtained from the LMDZ-iso model at very low resolution (VLR). **(j)** ERA5 air temperature at 850 hPa, with white lines marking front locations (see Fig. S1). **(k)** ERA5 vertical velocity plotted on a vertical cross section (altitude vs. longitude) along the transect indicated by the black dotted line in panel **(j)**.

extend this result here to the high-resolution temporal patterns of surface $\delta^{18}\text{O}_v$.

4.5 Synthesis

Figure 9 summarizes the proposed mechanism for negative $\delta^{18}\text{O}_v$ excursions as inferred from our data–model comparison when there is a clear rain event. A rain event is asso-

ciated with a strong ascending column in which $\delta^{18}\text{O}_v$ is depleted by progressive precipitation during the ascent and by interaction between rain and water vapor. This ascending column is generally associated with a cold front moving from southwest to northeast (Figs. 8j and S1), with subsidence and $\delta^{18}\text{O}_v$ -depleted air at the rear of the front (Figs. 8, S2, and S3).

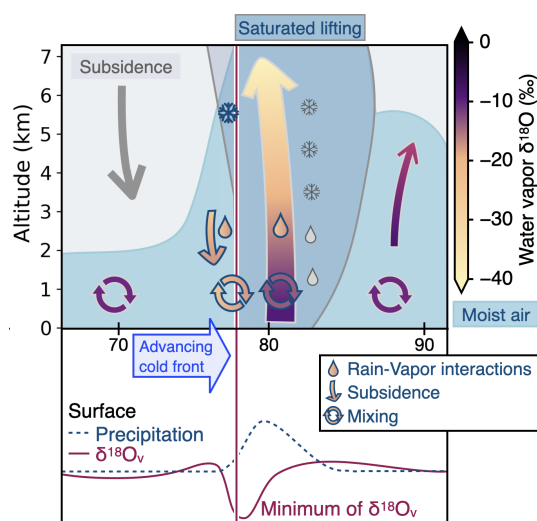


Figure 9. Scheme of the mechanism explaining the sharp negative excursion of $\delta^{18}\text{O}_v$ recorded at the surface for cold-front events associated with precipitation. The scheme is based on the profile modeled by ECHAM6-wiso for the event of 9 January 2020 (see Fig. S5 for the other events). The top panel shows the altitude vs. longitude dynamics of air masses with vertical saturated lifting in the center and subsidence at the rear of the lifting. The bottom panel shows the associated evolution of $\delta^{18}\text{O}_v$ and precipitation on the same longitude scale as the upper panel.

5 Conclusion

We presented here the first water vapor isotopic record over 2 years on Amsterdam Island. The water vapor isotopic variations follow at first order the variations of the water vapor mixing ratio, as expected for such a marine site. Superimposed on this variability, we have shown 11 periods of a few hours characterized by the occurrence of one or two abrupt negative excursions of $\delta^{18}\text{O}_v$, while the correlation between $\delta^{18}\text{O}_v$ and the water vapor mixing ratio does not hold. These negative excursions often occur toward the end of precipitation events. Most of the time they occur during a decrease in the water vapor mixing ratio. Representation of these short events is a challenge for the atmospheric components of Earth system models equipped with water isotopes, and we found that the ECHAM6-wiso model was able to reproduce most of the sharp negative $\delta^{18}\text{O}_v$ excursions, while the LMDZ-iso model at low (very low) resolution was only able to reproduce seven (one) of the negative excursions. The good agreement between modeled and measured $\delta^{18}\text{O}_v$ when using ECHAM6-wiso validates the physics processes within the ECHAM6-wiso model as well as the implemented physics of water isotopes.

Using previous modeling studies as well as information provided by (1) the confrontation with other data sources (GEM, meteorology) obtained in parallel on this site, (2) back-trajectory analyses, and (3) the outputs of the two models ECHAM6-wiso and LMDZ-iso, we conclude that the most plausible explanations for such events are rain–vapor interactions and subsidence at the rear of a precipitation event. Both can be combined, since rain–vapor interactions can help maintain moist conditions in subsidence regions.

This study highlights the added value of combining different data from a surface atmospheric observatory to understand the dynamics of the atmospheric circulation, e.g., subsidence in the higher atmosphere. These 2-year records are also a good benchmark for model evaluation. We have especially shown that the isotopic composition of water vapor measured at the surface is a powerful tool for testing the vertical dynamics of atmospheric models and the implementation of water isotopes for those that are equipped with them. In our case, we used it to test different horizontal resolutions which influence the representativity of the vertical dynamics and have important implications in the simulation of surface variations of water vapor $\delta^{18}\text{O}_v$. Our study highlights the importance of having high-resolution models (e.g., mesoscale models) equipped with isotopes to further study such abrupt isotopic events.

Appendix A

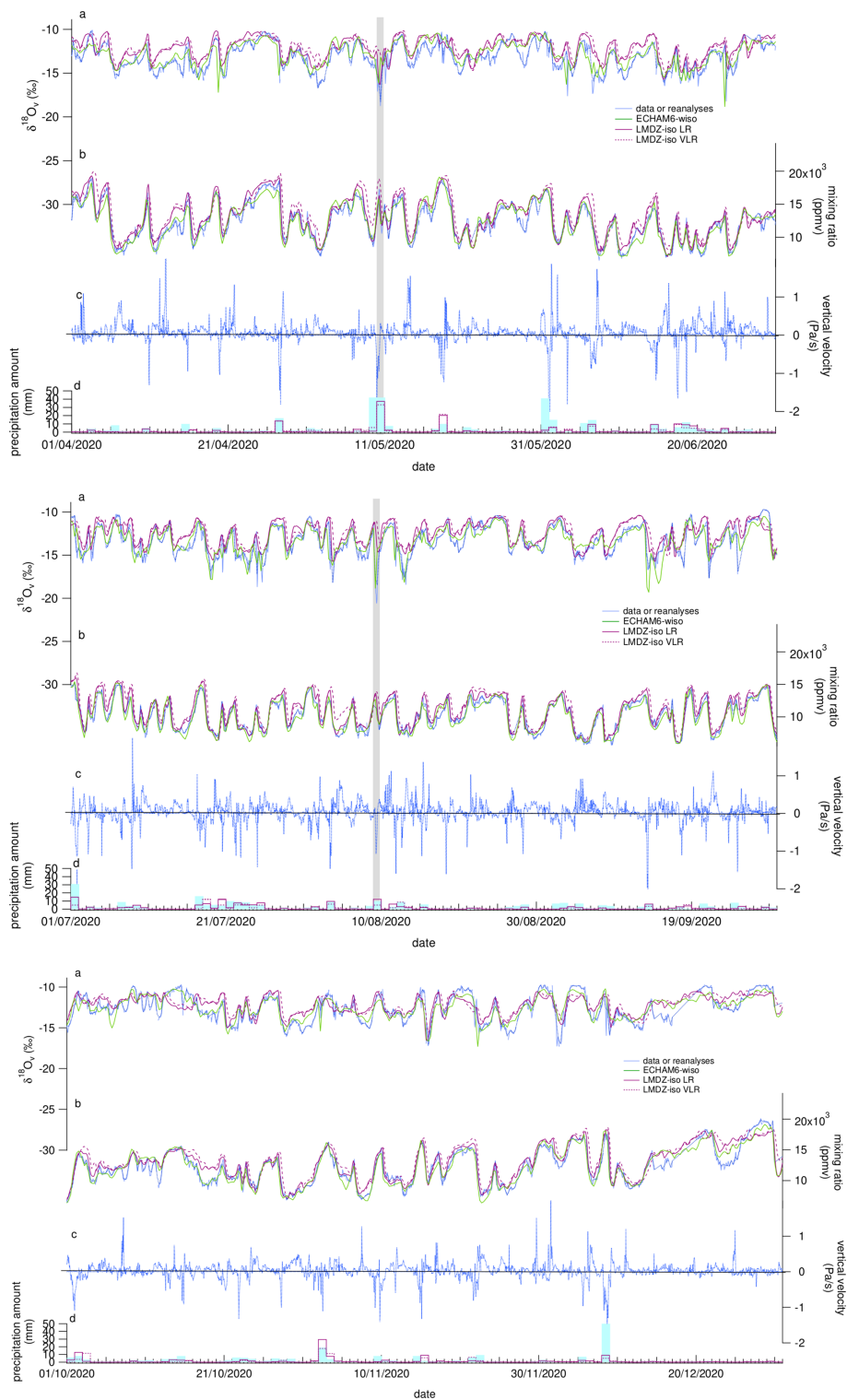


Figure A1.

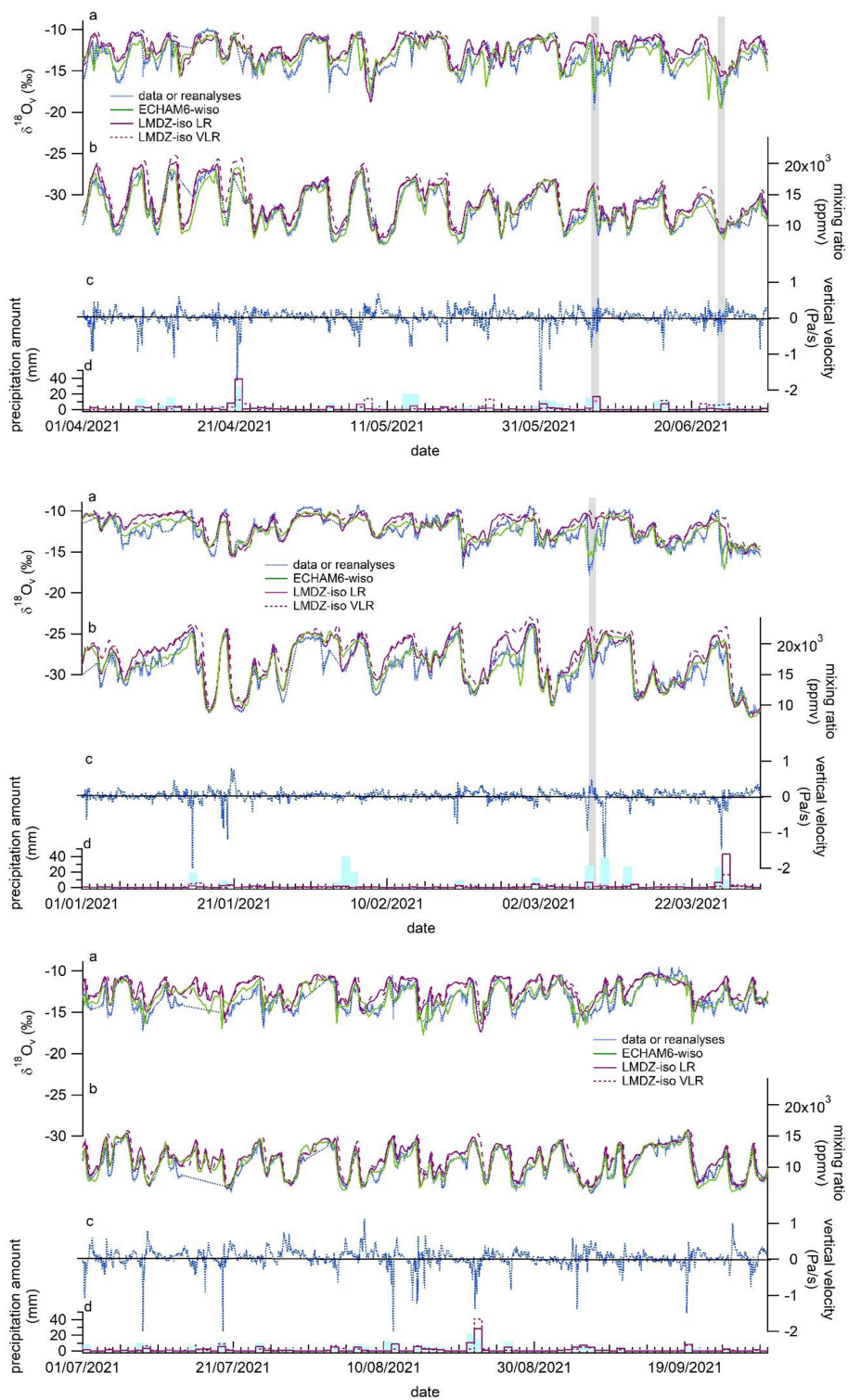


Figure A1.

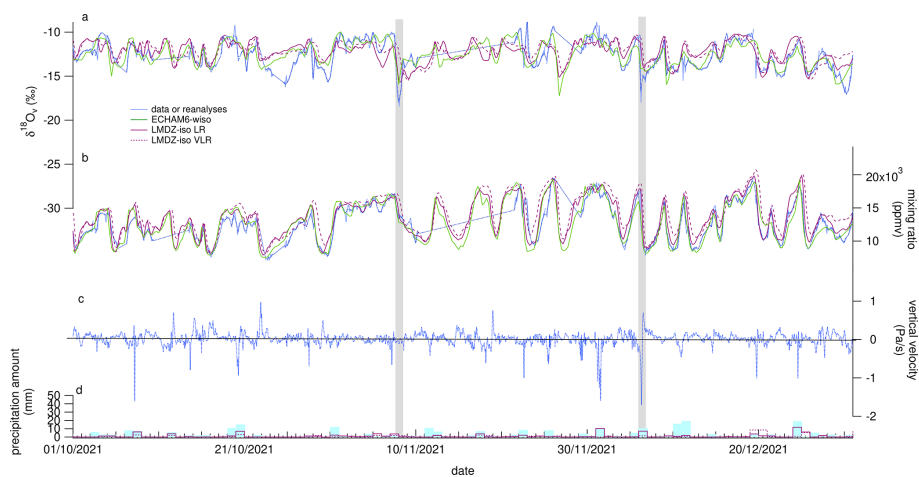


Figure A1. Model–measurement comparison (April 2020–December 2021). **(a)** $\delta^{18}\text{O}_v$ (light blue for data on an hourly average, dark blue for data resampled at a 6 h resolution). **(b)** Water vapor mixing ratio from our dataset. **(c)** Vertical velocity. **(d)** Precipitation amount. The grey shadings highlight the negative $\delta^{18}\text{O}_v$ excursions.

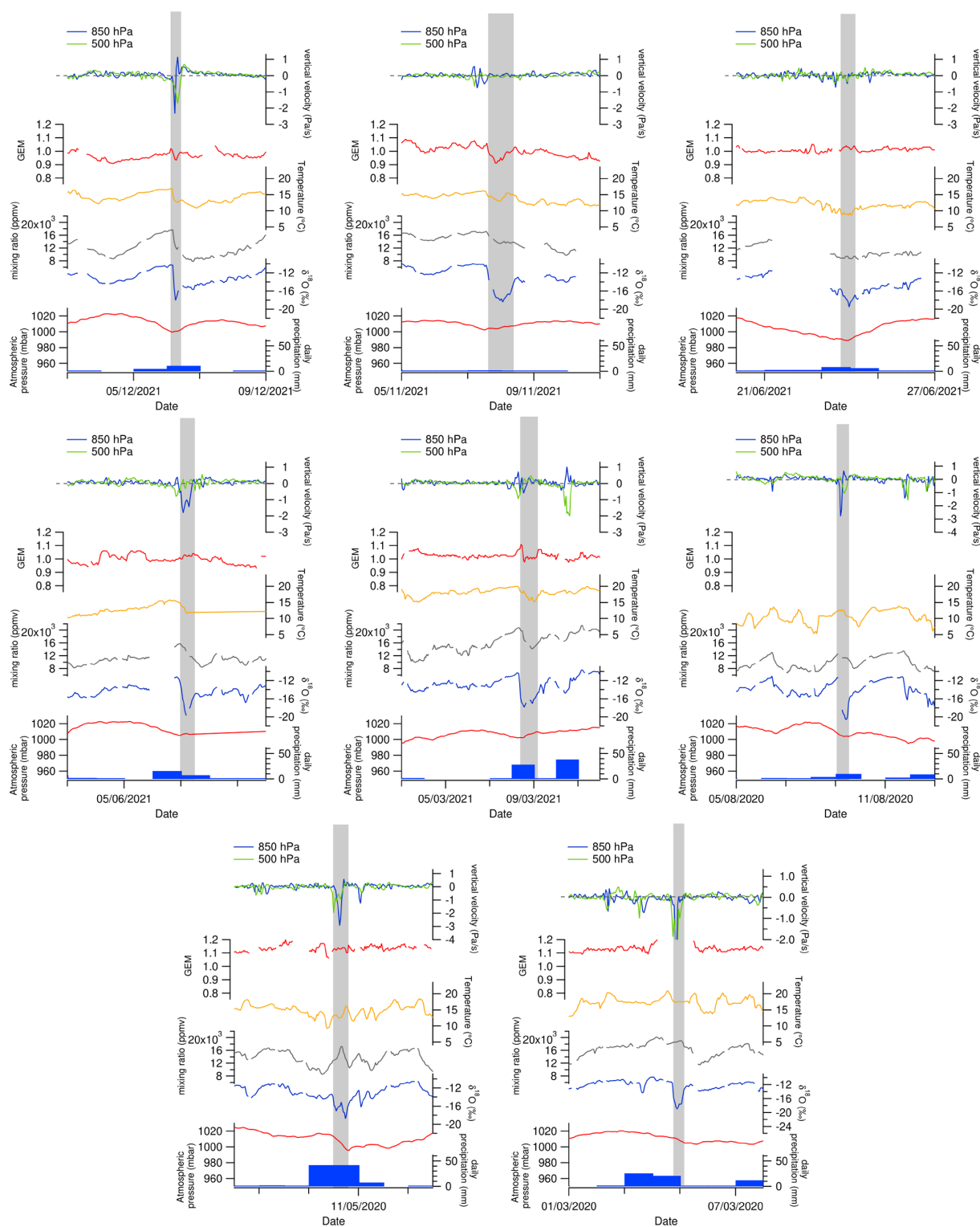


Figure A2. Evolution of GEM, $\delta^{18}O_v$, water vapor mixing ratio, meteorological parameters (surface temperature, surface atmospheric pressure, daily precipitation) measured by the Météo-France weather station, and vertical velocity from the ERA5 reanalyses at 500 and 850 hPa over the isotopic excursions between March 2020 and December 2021.

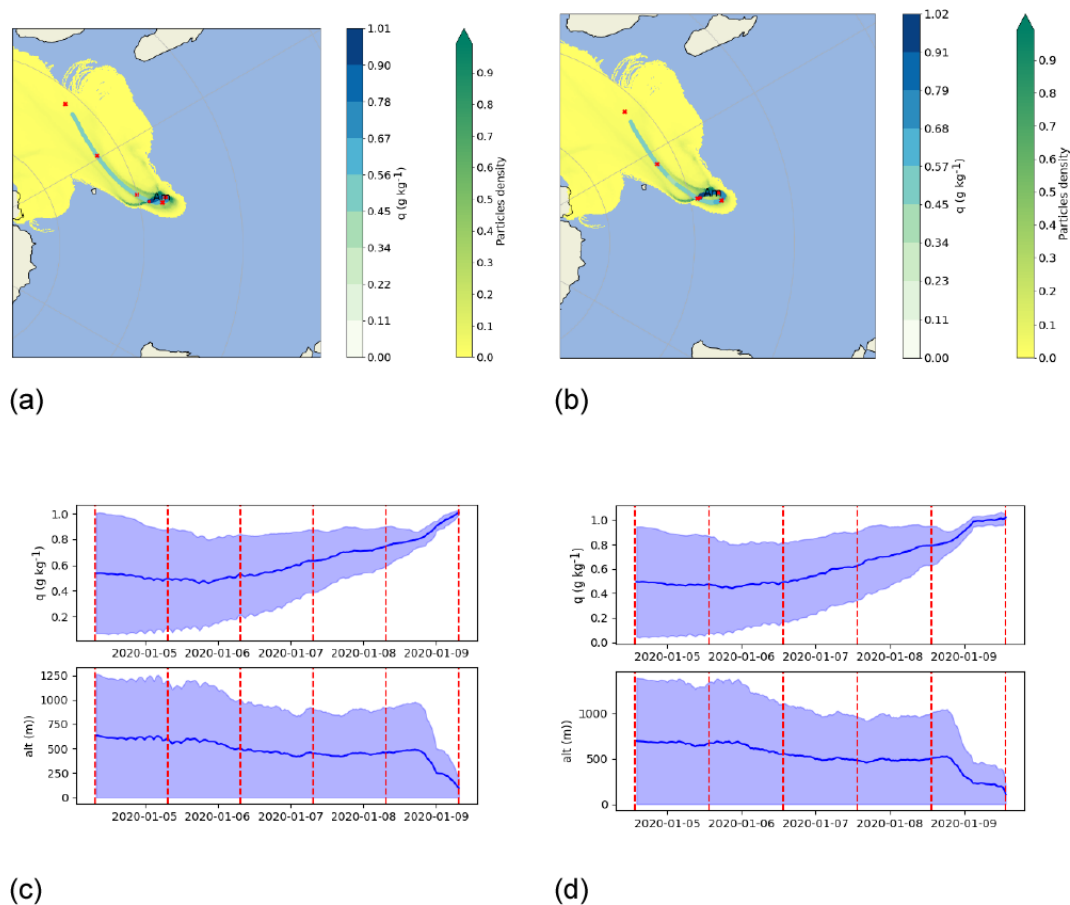


Figure A3. FLEXPART footprints of 5 d back trajectories for the event of 9 January 2020. **(a)** Latitude–longitude projection of the FLEXPART back-trajectory footprint for 9 January 2020 at 07:30. The yellow to green colors at each grid point of these projections represent the density of the particles. The white to blue colors indicate the water vapor mixing ratio on the humidity-weighted average back trajectory. Each red point indicates the location of the average back trajectory for each of the 5 d before the date of the considered event. **(b)** Same as for 9 January 2020 at 13:30. **(c)** The top shows the evolution of the water vapor mixing ratio of the back trajectories for 9 January 2020 at 07:30; the bottom shows the altitude evolution of the back trajectory for 9 January 2020 at 07:30. **(d)** Same as panel (c) for 9 January 2020 at 13:30.

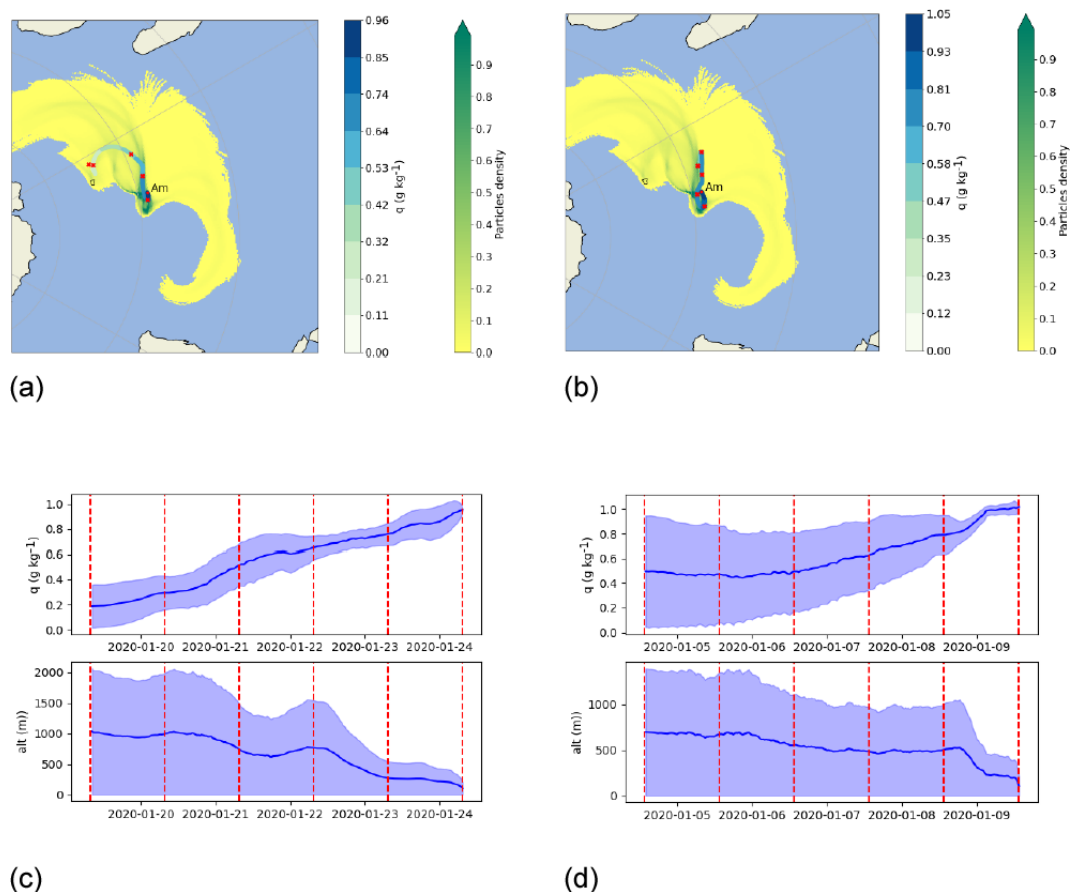


Figure A4. FLEXPART footprints of 5 d back trajectories for the event of 21 January 2020. **(a)** Latitude–longitude projection of the FLEXPART back-trajectory footprint for 21 January 2020 at 07:30. The yellow to green colors at each grid point of these projections represent the density of the particles. The white to blue colors indicate the water vapor mixing ratio on the humidity-weighted average back trajectory. Each red point indicates the location of the average back trajectory for all 5 d before the date of the considered event. **(b)** Same as for 21 January 2020 at 13:00. **(c)** The top shows the evolution of the water vapor mixing ratio of the back trajectories for 21 January 2020 at 07:30; the bottom shows the altitude evolution of the back trajectory for 21 January 2020 at 07:30. **(d)** Same as panel (c) for 21 January 2020 at 13:00.

Data availability. AMS L2 GEM data are freely available (<https://doi.org/10.25326/168>, Angot et al., 2023) from the national GMOS-FR website data portal coordinated by the IGE (Institut des Géosciences de l’Environnement, Grenoble, France) with the support of the French national AERIS-SEDOO partners, data and services center for the atmosphere. Hg species measurements belong to international monitoring networks as Global Observation System for Mercury (GOS4M). Water isotopic data and modeling outputs are available on the Zenodo platform (<https://doi.org/10.5281/zenodo.8164391>, Landais et al., 2023; <https://doi.org/10.5281/zenodo.8160596>, Cauquoin et al., 2023).

Supplement. The supplement related to this article is available online at: <https://doi.org/10.5194/acp-24-4611-2024-supplement>.

Author contributions. AL designed the study and analyzed the data together with FV, CS, EF, and OM. OC installed the water vapor isotopic analyzer on Amsterdam Island, and OJ was in charge of the data calibration. BM and FP performed the measurements of the isotopic composition of the precipitation samples. CA analyzed the modeling outputs, realized most of the simulations, and performed the model–data analyses. CLDS performed the back-trajectory analyses with the help of MC. OM, AD, and YB provided expertise on GEM analyses and interpretation. AC, CR, ND, and MW provided model simulations. AL wrote the paper with contributions from all the co-authors.

Competing interests. At least one of the (co-)authors is a member of the editorial board of *Atmospheric Chemistry and Physics*. The peer-review process was guided by an independent editor, and the authors also have no other competing interests to declare.

Disclaimer. Publisher's note: Copernicus Publications remains neutral with regard to jurisdictional claims made in the text, published maps, institutional affiliations, or any other geographical representation in this paper. While Copernicus Publications makes every effort to include appropriate place names, the final responsibility lies with the authors.

Acknowledgements. We gratefully thank all the overwintering staff at AMS and the French Polar Institute Paul-Emile Victor (IPEV) staff and scientists who helped with the setup and maintenance of the experiment at AMS in the framework of the GMOS_{Stral}-1028 IPEV program, the ICOS-416 program, and the ADELISE-1205 IPEV program. Amsterdam Island Hg₀ data accessible in the national GMOS-FR website data portal were collected via instruments coordinated by the IGE-PTICHA technical platform dedicated to atmospheric chemistry field instrumentation. The GMOS-FR data portal is maintained by the French national center for atmospheric data and services (AERIS), which is acknowledged by the authors. The LMDZ-iso simulations were performed thanks to granted access to the HPC resources of IDRIS under the allocations 2022-AD010114000 and 2022-AD010107632R1 made by GENCI. We gratefully thank Sébastien Nguyen (CEA, LSCE) for his help and support in running the LMDZ-iso simulation. The ERA5 reanalysis files for the ECHAM6-wiso nudging have been provided by the German Climate Computing Center (DKRZ). The ECHAM6-wiso simulations have been performed with the support of the Alfred Wegener Institute (AWI) supercomputing center.

Financial support. This work has benefited from the IPSL-CGS EUR and has been supported by a grant from the French government under the Programme d'Investissements d'avenir, reference ANR-11-IDEX-0004-17-EURE-0006, managed by the Agence Nationale de la Recherche. This project has also been supported by the LEFE IMAGO project ADELISE. Amsterdam Island GEM data, accessible in the national GMOS-FR website data portal, have been collected with funding from the European Union 7th Framework Programme project Global Mercury Observation System (GMOS 2010-2015 no. 26511), the IPEV through the GMOS_{Stral}-1028 IPEV program since 2012, the LEFE CHAT CNRS/INSU (TOPMODEL project no. AO2017-984931), and the H2020 ERA-PLANET (no. 689443) iGOSP program. This work is part of the AWACA project that has received funding from the European Research Council (ERC) under the European Union's Horizon 2020 research and innovation program (grant agreement no. 951596).

Review statement. This paper was edited by Farahnaz Khosrawi and reviewed by two anonymous referees.

References

Aemisegger, F., Sturm, P., Graf, P., Sodemann, H., Pfahl, S., Knohl, A., and Wernli, H.: Measuring variations of $\delta^{18}\text{O}$ and $\delta^2\text{H}$ in atmospheric water vapour using two commercial laser-based spectrometers: an instrument characterisation study, *Atmos. Meas.*

Tech., 5, 1491–1511, <https://doi.org/10.5194/amt-5-1491-2012>, 2012.

- Aemisegger, F., Spiegel, J., Pfahl, S., Sodemann, H., Eugster, W., and Wernli, H.: Isotope meteorology of cold front passages: A case study combining observations and modeling, *Geophys. Res. Lett.*, 42, 5652–5660, 2015.
- Angot, H., Barret, M., Magand, O., Ramonet, M., and Dommergue, A.: A 2-year record of atmospheric mercury species at a background Southern Hemisphere station on Amsterdam Island, *Atmos. Chem. Phys.*, 14, 11461–11473, <https://doi.org/10.5194/acp-14-11461-2014>, 2014.
- Angot, H., Dion, I., Vogel, N., Legrand, M., Magand, O., and Dommergue, A.: Multi-year record of atmospheric mercury at Dumont d'Urville, East Antarctic coast: continental outflow and oceanic influences, *Atmos. Chem. Phys.*, 16, 8265–8279, <https://doi.org/10.5194/acp-16-8265-2016>, 2016.
- Angot, H., Dommergue, A., Magand, O., and Bertrand, Y.: Continuous measurements of atmospheric mercury at Amsterdam Island (L2), AERIS [data set], <https://doi.org/10.25326/168>, 2023.
- Ansari, M. A., Noble, J., Deodhar, A., and Kumar, U. S.: Atmospheric factors controlling the stable isotopes ($\delta^{18}\text{O}$ and $\delta^2\text{H}$) of the Indian summer monsoon precipitation in a drying region of Eastern India, *J. Hydrol.*, 584, 124636, <https://doi.org/10.1016/j.jhydrol.2020.124636>, 2020.
- Arias, P. A., Bellouin, N., Coppola, E., Jones, R. G., Krinner, G., Marotzke, J., Naik, V., Palmer, M. D., Plattner, G.-K., Rogelj, J., Rojas, M., Sillmann, J., Storelvmo, T., Thorne, P. W., Trewin, B., Achuta Rao, K., Adhikary, B., Allan, R. P., Armour, K., Bala, G., Barimalala, R., Berger, S., Canadell, J. G., Cassou, C., Cherchi, A., Collins, W., Collins, W., Connors, S., Corti, S., Cruz, F., Dentener, F. J., Dereczynski, C., Di Luca, A., Diongue Niang, A., Doblus-Reyes, F. J., Dosio, A., Douville, H., Engelbrecht, F., Eyring, V., Fischer, E., Forster, P., Fox-Kemper, B., Fuglestedt, J., Fyfe, J., Gillett, N. P., Goldfarb, L., Gorodetskaya, I., Gutierrez, J. M., Hamdi, R., Hawkins, E., Hewitt, H. T., Hope, P., Islam, A. S., Jones, C., Kaufman, D., Kopp, R. E., Kosaka, Y., Kossin, J., Krakovska, S., Lee, J.-Y., Li, J., Mauritsen, T., Maycock, T. K., Meinshausen, M., Min, S.-K., Monteiro, P. M. S., Ngo-Duc, T., Otto, F., Pinto, I., Pirani, A., Raghavan, K., Ranasinghe, R., Ruane, A. C., Ruiz, L., Sallée, J.-B., Samsel, B. H., Sathyendranath, H., Seneviratne, S. I., Sörensson, A. A., Szopa, S., Takayabu, I., Tréguier, A.-M., van den Hurk, B., Vautard, R., von Schuckmann, K., Zaehle, S., Zhang, X., and Zickfeld, K.: *Climate Change 2021: the physical science basis. Contribution of Working Group I to the Sixth Assessment Report of the Intergovernmental Panel on Climate Change, technical summary*, <https://doi.org/10.1017/9781009157896.002>, 2021.
- Bailey, A., Aemisegger, F., Villiger, L., Los, S. A., Reverdin, G., Quiñones Meléndez, E., Acquistapace, C., Baranowski, D. B., Böck, T., Bony, S., Bordsdorff, T., Coffman, D., de Szoeké, S. P., Diekmann, C. J., Dütsch, M., Ertl, B., Galewsky, J., Henze, D., Makuch, P., Noone, D., Quinn, P. K., Rösch, M., Schneider, A., Schneider, M., Speich, S., Stevens, B., and Thompson, E. J.: Isotopic measurements in water vapor, precipitation, and seawater during EUREC4A, *Earth Syst. Sci. Data*, 15, 465–495, <https://doi.org/10.5194/essd-15-465-2023>, 2023.
- Benetti, M., Reverdin, G., Pierre, C., Merlivat, L., Risi, C., Steenlarsen, H. C., and Vimeux, F.: Deuterium excess in marine water vapor: Dependency on relative humidity and surface wind

- speed during evaporation, *J. Geophys. Res.-Atmos.*, 119, 584–593, <https://doi.org/10.1002/2013JD020535>, 2014.
- Benetti, M., Aloisi, G., Reverdin, G., Risi, C., and Sèze, G.: Importance of boundary layer mixing for the isotopic composition of surface vapor over the subtropical North Atlantic Ocean, *J. Geophys. Res.-Atmos.*, 120, 2190–2209, 2015.
- Bhattacharya, S. K., Sarkar, A., and Liang, M.-C.: Vapor isotope probing of typhoons invading the Taiwan region in 2016, *J. Geophys. Res.-Atmos.*, 127, e2022JD036578, <https://doi.org/10.1029/2022JD036578>, 2022.
- Bloom, N. and Fitzgerald, W. F.: Determination of volatile mercury species at the picogram level by low-temperature gas chromatography with cold-vapour atomic fluorescence detection, *Anal. Chim. Acta*, 208, 151–161, 1988.
- Bonne, J. L., Behrens, M., Meyer, H., Kipfstuhl, S., Rabe, B., Schönicke, L., Steen-Larsen, H. C., and Werner, M.: Resolving the controls of water vapour isotopes in the Atlantic sector, *Nat. Commun.*, 10, 1–10, <https://doi.org/10.1038/s41467-019-09242-6>, 2019.
- Boucher, O., Servonnat, J., Albright, A. L., Aumont, O., Balkanski, Y., Bastrikov, V., Bekki, S., Bonnet, R., Bony, S., Bopp, L., Braconnot, P., Brockmann, P., Cadule, P., Caubel, A., Cheruy, F., Codron, F., Cozic, A., Cugnet, D., D'Andrea, F., Davini, P., de Lavergne, C., Denvil, S., Deshayes, J., Devilliers, M., Ducharne, A., Dufresne, J.-L., Dupont, E., Éthé, C., Fairhead, L., Falletti, L., Flavoni, S., Foujols, M.-A., Gardoll, S., Gastineau, G., Ghattas, J., Grandpeix, J.-Y., Guenet, B., Guez, E., Lionel, Guilyardi, E., Guimberteau, M., Hauglustaine, D., Hourdin, F., Idelkadi, A., Joussaume, S., Kageyama, M., Khodri, M., Krinner, G., Lebas, N., Levvasseur, G., Lévy, C., Li, L., Lott, F., Lurton, T., Luysaert, S., Madec, G., Madeleine, J.-B., Maignan, F., Marchand, M., Marti, O., Mellul, L., Meurdesoif, Y., Mignot, J., Musat, I., Ottlé, C., Peylin, P., Planton, Y., Polcher, J., Rio, C., Rochetin, N., Rousset, C., Sepulchre, P., Sima, A., Swingedouw, D., Thiéblemont, R., Traore, A. K., Vancoppenolle, M., Vial, J., Vialard, J., Viovy, N., and Vuichard, N.: Presentation and Evaluation of the IPSL-CM6A-LR Climate Model, *J. Adv. Model. Earth Sy.*, 12, e2019MS002010, <https://doi.org/10.1029/2019MS002010>, 2020.
- Bréant, C., Leroy Dos Santos, C., Agosta, C., Casado, M., Fourré, E., Goursaud, S., Masson-Delmotte, V., Favier, V., Cattani, O., Prié, F., Golly, B., Orsi, A., Martinerie, P., and Landais, A.: Coastal water vapor isotopic composition driven by katabatic wind variability in summer at Dumont d'Urville, coastal East Antarctica, *Earth Planet. Sc. Lett.*, 514, 37–47, <https://doi.org/10.1016/j.epsl.2019.03.004>, 2019.
- Brooks, S., Ren, X. R., Cohen, M., Luke, W. T., Kelley, P., Artz, R., Hynes, A., Landing, W., and Martos, B.: Airborne vertical profiling of mercury speciation near Tullahoma, TN, USA, *Atmosphere*, 5, 557–574, <https://doi.org/10.3390/atmos5030557>, 2014.
- Casado, M., Landais, A., Masson-Delmotte, V., Genthon, C., Kerstel, E., Kassi, S., Arnaud, L., Picard, G., Prie, F., Cattani, O., Steen-Larsen, H.-C., Vignon, E., and Cermak, P.: Continuous measurements of isotopic composition of water vapour on the East Antarctic Plateau, *Atmos. Chem. Phys.*, 16, 8521–8538, <https://doi.org/10.5194/acp-16-8521-2016>, 2016.
- Cauquoin, A. and Werner, M.: High-Resolution Nudged Isotope Modeling With ECHAM6-Wiso: Impacts of Updated Model Physics and ERA5 Reanalysis Data, *J. Adv. Model. Earth Sy.*, 13, e2021MS002532, <https://doi.org/10.1029/2021MS002532>, 2021.
- Cauquoin, A., Werner, M., and Lohmann, G.: Water isotopes – climate relationships for the mid-Holocene and preindustrial period simulated with an isotope-enabled version of MPI-ESM, *Clim. Past*, 15, 1913–1937, <https://doi.org/10.5194/cp-15-1913-2019>, 2019.
- Cauquoin, A., Werner, M., Risi, C., Dutrievoz, N., and Agosta, C.: Modeling abrupt excursions in water vapor isotopic variability during cold fronts at the Pointe Benedicte observatory in Amsterdam Island/Model dataset, Version 0.1, Zenodo [data set], <https://doi.org/10.5281/zenodo.8160596>, 2023.
- Ciais, P. and Jouzel, J.: Deuterium and oxygen 18 in precipitation: Isotopic model, including mixed cloud processes, *J. Geophys. Res.-Atmos.*, 99, 16793–16803, 1994.
- Craig, H.: Isotopic Variations in Meteoric Waters, *Science*, 133, 1702–1703, <https://doi.org/10.1126/science.133.3465.1702>, 1961.
- Dahinden, F., Aemisegger, F., Wernli, H., Schneider, M., Diekmann, C. J., Ertl, B., Knippertz, P., Werner, M., and Pfahl, S.: Disentangling different moisture transport pathways over the eastern subtropical North Atlantic using multi-platform isotope observations and high-resolution numerical modelling, *Atmos. Chem. Phys.*, 21, 16319–16347, <https://doi.org/10.5194/acp-21-16319-2021>, 2021.
- Dansgaard, W.: Stable isotopes in precipitation, *Tellus*, 16, 436–468, 1964.
- Dumarey, R., Temmerman, E., Adams, R., and Hoste, J.: The accuracy of the vapour-injection calibration method for the determination of mercury by amalgamation/cold-vapour atomic absorption spectrometry, *Anal. Chim. Acta*, 170, 337–340, 1985.
- Durack, P. J., Taylor, K. E., Ames, S., Po-Chedley, S., and Mauzey, C.: PCMDI AMIP SST and sea-ice boundary conditions version 1.1.8, Earth System Grid Federation [data set], <https://doi.org/10.22033/ESGF/input4MIPs.16921>, 2022.
- Dütsch, M., Pfahl, S., and Wernli, H.: Drivers of $\delta^2\text{H}$ variations in an idealized extratropical cyclone, *Geophys. Res. Lett.*, 43, 5401–5408, 2016.
- Edwards, B. A., Kushner, D. S., Outridge, P. M., and Wang, F.: Fifty years of volcanic mercury emission research: Knowledge gaps and future directions, *Sci. Total Environ.*, 757, 143800, <https://doi.org/10.1016/j.scitotenv.2020.143800>, 2021.
- El Yazidi, A., Ramonet, M., Ciais, P., Broquet, G., Pison, I., Abbaris, A., Brunner, D., Conil, S., Delmotte, M., Gheusi, F., Guerin, F., Hazan, L., Kachroudi, N., Kouvarakis, G., Mihalopoulos, N., Rivier, L., and Serça, D.: Identification of spikes associated with local sources in continuous time series of atmospheric CO, CO₂ and CH₄, *Atmos. Meas. Tech.*, 11, 1599–1614, <https://doi.org/10.5194/amt-11-1599-2018>, 2018.
- Eyring, V., Bony, S., Meehl, G. A., Senior, C. A., Stevens, B., Stouffer, R. J., and Taylor, K. E.: Overview of the Coupled Model Intercomparison Project Phase 6 (CMIP6) experimental design and organization, *Geosci. Model Dev.*, 9, 1937–1958, <https://doi.org/10.5194/gmd-9-1937-2016>, 2016.
- Faïn, X., Obrist, D., Hallar, A. G., Mccubbin, I., and Rahn, T.: High levels of reactive gaseous mercury observed at a high elevation research laboratory in the Rocky Mountains, *Atmos. Chem.*

- Phys., 9, 8049–8060, <https://doi.org/10.5194/acp-9-8049-2009>, 2009.
- Fitzgerald, W. F. and Gill, G. A.: Subnanogram determination of mercury by two-stage gold amalgamation and gas phase detection applied to atmospheric analysis, *Anal. Chem.*, 51, 1714–1720, 1979.
- Fu, X., Maruszczak, N., Wang, X., Gheusi, F. and Sonke, J.: The isotopic composition of gaseous elemental mercury in the free troposphere of the Pic du Midi Observatory, France, *Environ. Sci. Technol.*, 50, 5641–5650, <https://doi.org/10.1021/acs.est.6b00033>, 2016.
- Galewsky, J., Steen-Larsen, H. C., Field, R. D., Worden, J., Risi, C., and Schneider, M.: Stable isotopes in atmospheric water vapor and applications to the hydrologic cycle, *Rev. Geophys.*, 54, 809–865, 2016.
- Gaudry, A., Ascencio, J., and Lambert, G.: Preliminary study of CO₂ variations at Amsterdam Island (Territoire des Terres Australes et Antarctiques Françaises), *J. Geophys. Res.-Oceans*, 88, 1323–1329, 1983.
- Graf, P., Wernli, H., Pfahl, S., and Sodemann, H.: A new interpretative framework for below-cloud effects on stable water isotopes in vapour and rain, *Atmos. Chem. Phys.*, 19, 747–765, <https://doi.org/10.5194/acp-19-747-2019>, 2019.
- Gros, V., Poisson, N., Martin, D., Kanakidou, M., and Bonsang, B.: Observations and modeling of the seasonal variation of surface ozone at Amsterdam Island: 1994–1996, *J. Geophys. Res.-Atmos.*, 103, 28103–28109, 1998.
- Gros, V., Bonsang, B., Martin, D., Novelli, P., and Kazan, V.: Carbon monoxide short term measurements at Amsterdam island: estimations of biomass burning emission rates, *Chemosphere-Global Change Science*, 1, 163–172, 1999.
- Gaffney, J. and Marley, N.: In-depth review of atmospheric mercury: sources, transformations, and potential sinks, *Energy and Emission Control Technologies*, 2014, 1–21, <https://doi.org/10.2147/EECT.S37038>, 2014.
- Guilpart, E., Vimeux, F., Evan, S., Brioude, J., Metzger, J., Barthe, C., Risi, C., and Cattani, O.: The isotopic composition of near-surface water vapor at the Maïdo observatory (Reunion Island, southwestern Indian Ocean) documents the controls of the humidity of the subtropical troposphere, *J. Geophys. Res.-Atmos.*, 122, 9628–9650, <https://doi.org/10.1002/2017JD026791>, 2017.
- Gustin, M. S., Amos, H. M., Huang, J., Miller, M. B., and Heidecorn, K.: Measuring and modeling mercury in the atmosphere: a critical review, *Atmos. Chem. Phys.*, 15, 5697–5713, <https://doi.org/10.5194/acp-15-5697-2015>, 2015.
- Gustin, M. S., Bank, M. S., Bishop, K., Bowman, K., Brafireun, B., Chételat, J., Eckley, C. S., Hammerschmidt, C. R., Lamborg, C., Lyman, S., Martínez-Cortizas, A., Sommar, J., Tsz-Ki Tsui, M., and Zhang, T.: Mercury biogeochemical cycling: A synthesis of recent scientific advances, *Sci. Total Environ.*, 737, 139619, <https://doi.org/10.1016/j.scitotenv.2020.139619>, 2020.
- Gworek, B., Dmuchowski, W., and Baczevska-Dąbrowska, A. H.: Mercury in the terrestrial environment: a review, *Environ. Sci. Eur.*, 32, 128, <https://doi.org/10.1186/s12302-020-00401-x>, 2020.
- Henze, D., Noone, D., and Toohey, D.: Aircraft measurements of water vapor heavy isotope ratios in the marine boundary layer and lower troposphere during ORACLES, *Earth Syst. Sci. Data*, 14, 1811–1829, <https://doi.org/10.5194/essd-14-1811-2022>, 2022.
- Hersbach, H., Bell, B., Berrisford, P., Hirahara, S., Horányi, A., Muñoz-Sabater, J., Nicolas, J., Peubey, C., Radu, R., Schepers, D., Simmons, A., Soci, C., Abdalla, S., Abellan, X., Balsamo, G., Bechtold, P., Biavati, G., Bidlot, J., Bonavita, M., De Chiara, G., Dahlgren, P., Dee, D., Diamantakis, M., Dragani, R., Flemming, J., Forbes, R., Fuentes, M., Geer, A., Haimberger, L., Healy, S., Hogan, R. J., Hólm, E., Janisková, M., Keeley, S., Laloyaux, P., Lopez, P., Lupu, C., Radnoti, G., de Rosnay, P., Rozum, I., Vamborg, F., Villaume, S., and Thépaut, J.-N.: The ERA5 global reanalysis, *Q. J. Roy. Meteor. Soc.*, 146, 1999–2049, <https://doi.org/10.1002/qj.3803>, 2020.
- Hoang, C., Magand, O., Brioude, J., Dimuro, A., Brunet, C., Ah-Peng, C., Bertrand, Y., Dommergue, A., Lei, Y. D., and Wania, F.: Probing the limits of sampling gaseous elemental mercury passively in the remote atmosphere, *Environ. Sci.-Atmos.*, 3, 268–281, <https://doi.org/10.1039/D2EA00119E>, 2023.
- Hourdin, F., Rio, C., Grandpeix, J.-Y., Madeleine, J.-B., Cheruy, F., Rochetin, N., Jam, A., Musat, I., Idelkadi, A., Fairhead, L., Foujols, M.-A., Mellul, L., Traore, A.-K., Dufresne, J.-L., Boucher, O., Lefebvre, M.-P., Millour, E., Vignon, E., Jouhaud, J., Diallo, F. B., Lott, F., Gastineau, G., Caubel, A., Meurdesoif, Y., and Ghattas, J.: LMDZ6A: The Atmospheric Component of the IPSL Climate Model With Improved and Better Tuned Physics, *J. Adv. Model. Earth Sy.*, 12, e2019MS001892, <https://doi.org/10.1029/2019MS001892>, 2020.
- Jiskra, M., Sonke, J. E., Obrist, D., Bieser, J., Ebinghaus, R., Myhre, C. L., Pfaffhuber, K. A., Wängberg, I., Kyllönen, K., Worthy, D., Martin, L. G., Labuschagne, C., Mkololo, T., Ramonet, M., Magand, O., and Dommergue, A.: A vegetation control on seasonal variations in global atmospheric mercury concentrations, *Nat. Geosci.*, 11, 244–250, <https://doi.org/10.1038/s41561-018-0078-8>, 2018.
- Jullien, N., Vignon, É., Sprenger, M., Aemisegger, F., and Berne, A.: Synoptic conditions and atmospheric moisture pathways associated with virga and precipitation over coastal Adélie Land in Antarctica, *The Cryosphere*, 14, 1685–1702, <https://doi.org/10.5194/tc-14-1685-2020>, 2020.
- Koenig, A. M., Magand, O., Verreyken, B., Brioude, J., Aemlynck, C., Schoon, N., Colomb, A., Ferreira Araujo, B., Ramonet, M., Sha, M. K., Cammas, J.-P., Sonke, J. E., and Dommergue, A.: Mercury in the free troposphere and bidirectional atmosphere–vegetation exchanges – insights from Maïdo mountain observatory in the Southern Hemisphere tropics, *Atmos. Chem. Phys.*, 23, 1309–1328, <https://doi.org/10.5194/acp-23-1309-2023>, 2023.
- Landais, A., Fourné, E., Cattani, O., Minster, B., Jossoud, O., and Prié, F.: Modeling abrupt excursions in water vapor isotopic variability during cold fronts at the Pointe Benedicte observatory in Amsterdam Island/Observation dataset, Version v1, Zenodo [data set], <https://doi.org/10.5281/zenodo.8164391>, 2023.
- Lee, K.-O., Aemisegger, F., Pfahl, S., Flamant, C., Lacour, J.-L., and Chaboureaud, J.-P.: Contrasting stable water isotope signals from convective and large-scale precipitation phases of a heavy precipitation event in southern Italy during HyMeX IOP 13: a modelling perspective, *Atmos. Chem. Phys.*, 19, 7487–7506, <https://doi.org/10.5194/acp-19-7487-2019>, 2019.

- LeGrande, A. N. and Schmidt, G. A.: Global gridded data set of the oxygen isotopic composition in seawater, *Geophys. Res. Lett.*, 33, L12604, <https://doi.org/10.1029/2006GL026011>, 2006.
- Leroy-Dos Santos, C., Masson-Delmotte, V., Casado, M., Fourré, E., Steen-Larsen, H. C., Maturilli, M., Orsi, A., Berchet, A., Cattani, O., Minster, B., Gherardi, J., and Landais, A.: A 4.5 Year-Long Record of Svalbard Water Vapor Isotopic Composition Documents Winter Air Mass Origin, *J. Geophys. Res.-Atmos.*, 125, e2020JD032681, <https://doi.org/10.1029/2020JD032681>, 2020.
- Leroy-Dos Santos, C., Casado, M., Prié, F., Jossoud, O., Kerstel, E., Farradèche, M., Kassi, S., Fourré, E., and Landais, A.: A dedicated robust instrument for water vapor generation at low humidity for use with a laser water isotope analyzer in cold and dry polar regions, *Atmos. Meas. Tech.*, 14, 2907–2918, <https://doi.org/10.5194/amt-14-2907-2021>, 2021.
- Li, C., Enrico, M., Magand, O., Araujo, B. F., Le Roux, G., Osterwalder, S., Dommergue, A., Bertrand, Y., Brioude, J., De Vleeschouwer, F., and Sonke, J. E.: A peat core Hg stable isotope reconstruction of Holocene atmospheric Hg deposition at Amsterdam Island (37.8 oS), *Geochim. Cosmochim. Ac.*, 341, 62–74, 2023.
- Lindberg, S., Bullock, R., Ebinghaus, R., Engstrom, D., Feng, X., Fitzgerald, W., Pirrone, N., Prestbo, E., and Seigneur, C.: A synthesis of progress and uncertainties in attributing the sources of mercury in deposition, *Ambio*, 36, 19–32, <https://doi.org/10.1579/0044-7447.2007>.
- Lyman, S. N. and Jaffe, D. A.: Formation and fate of oxidized mercury in the upper troposphere and lower stratosphere, *Nat. Geosci.*, 5, 114–117, <https://doi.org/10.1038/ngeo1353> 2012.
- Markle, B. R. and Steig, E. J.: Improving temperature reconstructions from ice-core water-isotope records, *Clim. Past*, 18, 1321–1368, <https://doi.org/10.5194/cp-18-1321-2022>, 2022.
- Munksgaard, N. C., Zwart, C., Kurita, N., Bass, A., Nott, J., and Bird, M. I.: Stable isotope anatomy of tropical cyclone Ita, north-eastern Australia, April 2014, *PloS one*, 10, e0119728, <https://doi.org/10.1371/journal.pone.0119728>, 2015.
- Murphy, D. M., Hudson, P. K., Thomson, D. S., Sheridan, P. J., and Wilson, J. C.: Observations of Mercury-Containing Aerosols, *Environ. Sci. Technol.*, 40, 3163–3167, 2006.
- Noone, D.: Pairing Measurements of the Water Vapor Isotope Ratio with Humidity to Deduce Atmospheric Moistening and Dehydration in the Tropical Midtroposphere, *J. Climate*, 25, 4476–4494, <https://doi.org/10.1175/JCLI-D-11-00582.1>, 2012.
- Pisso, I., Sollum, E., Grythe, H., Kristiansen, N. I., Cassiani, M., Eckhardt, S., Arnold, D., Morton, D., Thompson, R. L., Groot Zwaafink, C. D., Evangeliou, N., Sodemann, H., Haimberger, L., Henne, S., Brunner, D., Burkhardt, J. F., Fouilloux, A., Brioude, J., Philipp, A., Seibert, P., and Stohl, A.: The Lagrangian particle dispersion model FLEX-PART version 10.4, *Geosci. Model Dev.*, 12, 4955–4997, <https://doi.org/10.5194/gmd-12-4955-2019>, 2019.
- Polian, G., Lambert, G., Ardouin, B., and Jegou, A.: Long-range transport of continental radon in subantarctic and antarctic areas, *Tellus B*, 38, 178–189, 1986.
- Risi, C., Bony, S., Vimeux, F., and Jouzel, J.: Water-stable isotopes in the LMDZ4 general circulation model: Model evaluation for present-day and past climates and applications to climatic interpretations of tropical isotopic records, *J. Geophys. Res.-Atmos.*, 115, D12118, <https://doi.org/10.1029/2009JD013255>, 2010.
- Ryan, B. F., Katzfey, J. J., Abbs, D. J., Jakob, C., Lohmann, U., Rockel, B., Rotstayn, L. D., Stewart, R. E., Szeto, K. K., Tselioudis, G., and Yau, M. K.: Simulations of a cold front by cloud-resolving, limited-area, and large-scale models, and a model evaluation using in situ and satellite observations, *Mon. Weather Rev.*, 128, 3218–3235, [https://doi.org/10.1175/1520-0493\(2000\)128<3218:SOACFB>2.0.CO;2](https://doi.org/10.1175/1520-0493(2000)128<3218:SOACFB>2.0.CO;2), 2000.
- Sciare, J., Mihalopoulos, N., and Dentener, F.: Interannual variability of atmospheric dimethylsulfide in the southern Indian Ocean, *J. Geophys. Res.-Atmos.*, 105, 26369–26377, 2000.
- Sciare, J., Favez, O., Sarda-Estève, R., Oikonomou, K., Cachier, H., and Kazan, V.: Long-term observations of carbonaceous aerosols in the Austral Ocean atmosphere: Evidence of a biogenic marine organic source, *J. Geophys. Res.-Atmos.*, 114, D15302, <https://doi.org/10.1029/2009JD011998>, 2009.
- Shah, V., Jacob, D. J., Thackray, C. P., Wang, X., Sunderland, E. M., Dibble, T. S., Saiz-Lopez, A., Cernušák, I., Kellö, V., Castro, P. J., Wu, R., and Wang, C.: Improved Mechanistic Model of the Atmospheric Redox Chemistry of Mercury, *Environ. Sci. Technol.*, 55, 14445–14456, <https://doi.org/10.1021/acs.est.1c03160>, 2021.
- Sheu, G. R., Lin, N. H., Wang, J. L., Lee, C. T., Yang, C. F. O., and Wang, S. H.: Temporal distribution and potential sources of atmospheric mercury measured at a high-elevation background station in Taiwan, *Atmos. Environ.*, 44, 2393–2400, <https://doi.org/10.1016/j.atmosenv.2010.04.009>, 2010.
- Sherwood, S. C., Bony, S., and Dufresne, J.-L.: Spread in model climate sensitivity traced to atmospheric convective mixing, *Nature*, 505, 37–42, <https://doi.org/10.1038/nature12829>, 2014.
- Sillman, S., Marsik, F. J., Al-Wali, K. I., Keeler, G. J., and Landis, M. S.: Reactive mercury in the troposphere: Model formation and results for Florida, the northeastern United States, and the Atlantic Ocean, *J. Geophys. Res.-Atmos.*, 112, D23305, <https://doi.org/10.1029/2006JD008227>, 2007.
- Slemr, F., Angot, H., Dommergue, A., Magand, O., Barret, M., Weigelt, A., Ebinghaus, R., Brunke, E.-G., Pfaffhuber, K. A., Edwards, G., Howard, D., Powell, J., Keywood, M., and Wang, F.: Comparison of mercury concentrations measured at several sites in the Southern Hemisphere, *Atmos. Chem. Phys.*, 15, 3125–3133, <https://doi.org/10.5194/acp-15-3125-2015>, 2015.
- Slemr, F., Martin, L., Labuschagne, C., Mkololo, T., Angot, H., Magand, O., Dommergue, A., Garat, P., Ramonet, M., and Bieser, J.: Atmospheric mercury in the Southern Hemisphere – Part 1: Trend and inter-annual variations in atmospheric mercury at Cape Point, South Africa, in 2007–2017, and on Amsterdam Island in 2012–2017, *Atmos. Chem. Phys.*, 20, 7683–7692, <https://doi.org/10.5194/acp-20-7683-2020>, 2020.
- Sprovieri, F., Pirrone, N., Bencardino, M., D’Amore, F., Carbone, F., Cinnirella, S., Mannarino, V., Landis, M., Ebinghaus, R., Weigelt, A., Brunke, E.-G., Labuschagne, C., Martin, L., Munthe, J., Wängberg, I., Artaxo, P., Morais, F., Barbosa, H. D. M. J., Brito, J., Cairns, W., Barbante, C., Diéguez, M. D. C., Garcia, P. E., Dommergue, A., Angot, H., Magand, O., Skov, H., Horvat, M., Kotnik, J., Read, K. A., Neves, L. M., Gawlik, B. M., Sena, F., Mashyanov, N., Obolkin, V., Wip, D., Feng, X. B., Zhang, H., Fu, X., Ramachandran, R., Cossa, D., Knoery, J., Maruszczak, N., Nerentorp, M., and Norstrom,

- C.: Atmospheric mercury concentrations observed at ground-based monitoring sites globally distributed in the framework of the GMOS network, *Atmos. Chem. Phys.*, 16, 11915–11935, <https://doi.org/10.5194/acp-16-11915-2016>, 2016.
- Steen-Larsen, H. C., Johnsen, S. J., Masson-Delmotte, V., Stenni, B., Risi, C., Sodemann, H., Balslev-Clausen, D., Blunier, T., Dahl-Jensen, D., Ellehøj, M. D., Falourd, S., Grinsted, A., Gkinis, V., Jouzel, J., Popp, T., Sheldon, S., Simonsen, S. B., Sjolte, J., Steffensen, J. P., Sperlich, P., Sveinbjörnsdóttir, A. E., Vinther, B. M., and White, J. W. C.: Continuous monitoring of summer surface water vapor isotopic composition above the Greenland Ice Sheet, *Atmos. Chem. Phys.*, 13, 4815–4828, <https://doi.org/10.5194/acp-13-4815-2013>, 2013.
- Steffen, A., Scherz, T., Olson, M., Gay, D., and Blanchard, P.: A comparison of data quality control protocols for atmospheric mercury speciation measurements, *J. Environ. Monitor.*, 14, 752–765, 2012.
- Stevens, B., Giorgetta, M., Esch, M., Mauritsen, T., Crueger, T., Rast, S., Salzmann, M., Schmidt, H., Bader, J., Block, K., Brokopf, R., Fast, I., Kinne, S., Kornblüeh, L., Lohmann, U., Pincus, R., Reichler, T., and Roeckner, E.: Atmospheric component of the MPI-M Earth System Model: ECHAM6, *J. Adv. Model. Earth Sy.*, 5, 146–172, <https://doi.org/10.1002/jame.20015>, 2013.
- Swartzendruber, P., Chand, D., Jaffe, D., Smith, J., Reidmiller, D., Gratz, L., Keeler, J., Strode, S., Jaeglé, L., and Talbot, R.: Vertical distribution of mercury, CO, ozone, and aerosol scattering coefficient in the Pacific Northwest during the spring 2006 INTEX-B campaign, *J. Geophys. Res.-Atmos.*, 113, D10305, <https://doi.org/10.1029/2007JD009579>, 2008.
- Swartzendruber, P. C., Jaffe, D. A., Prestbo, E., Weiss-Penzias, P., Selin, N. E., Park, R., Jacob, D. J., Strode, S., and Jaegle, L.: Observations of reactive gaseous mercury in the free troposphere at the Mount Bachelor Observatory, *J. Geophys. Res.-Atmos.*, 111, D24301, <https://doi.org/10.1029/2006JD007415>, 2006.
- Swartzendruber, P., Chand, D., Jaffe, D. A., Smith, J., Reidmiller, D., Gratz, L., Keeler, J., Strode, S., Jaegle, L., and Talbot, R.: Vertical distribution of mercury, CO, ozone, and aerosol scattering coefficient in the Pacific Northwest during the spring 2006 INTEX-B campaign, *J. Geophys. Res.-Atmos.*, 113, D10305, <https://doi.org/10.1029/2007JD009579>, 2008.
- Talbot, R., Mao, H., Scheuer, E., Dibb, J., and Avery, M.: Total depletion of Hg in the upper troposphere–lower stratosphere, *Geophys. Res. Lett.*, 34, L23804, <https://doi.org/10.1029/2007GL031366>, 2007.
- Talbot, R., Mao, H., Scheuer, E., Dibb, J., Avery, M., Browell, E., Sachse, G., Vay, S., Blake, D., Huey, G., and Fuelberg, H.: Factors influencing the large-scale distribution of Hg⁰ in the Mexico City area and over the North Pacific, *Atmos. Chem. Phys.*, 8, 2103–2114, <https://doi.org/10.5194/acp-8-2103-2008>, 2008.
- Taylor, K. E., Williamson, D., and Zwiers, F.: The sea surface temperature and sea ice concentration boundary conditions for AMIP II simulations, PCMDI Report 60, Program for Climate Model Diagnosis and Intercomparison, Lawrence Livermore National Laboratory, <https://pcmdi.llnl.gov/report/ab60.html> (last access: 8 April 2024), 2000.
- Thurnherr, I., Kozachek, A., Graf, P., Weng, Y., Bolshiyarov, D., Landwehr, S., Pfahl, S., Schmale, J., Sodemann, H., Steen-Larsen, H. C., Toffoli, A., Wernli, H., and Aemisegger, F.: Meridional and vertical variations of the water vapour isotopic composition in the marine boundary layer over the Atlantic and Southern Ocean, *Atmos. Chem. Phys.*, 20, 5811–5835, <https://doi.org/10.5194/acp-20-5811-2020>, 2020.
- Tremoy, G., Vimeux, F., Cattani, O., Mayaki, S., Souley, I., and Favreau, G.: Measurements of water vapor isotope ratios with wavelength-scanned cavity ring-down spectroscopy technology: New insights and important caveats for deuterium excess measurements in tropical areas in comparison with isotope-ratio mass spectrometry, *Rapid Commun. Mass Sp.*, 25, 3469–3480, <https://doi.org/10.1002/rcm.5252>, 2011.
- Tremoy, G., Vimeux, F., Mayaki, S., Souley, I., Cattani, O., Risi, C., Favreau, G., and Oi, M.: A 1-year long $\delta^{18}\text{O}$ record of water vapor in Niamey (Niger) reveals insightful atmospheric processes at different timescales, *Geophys. Res. Lett.*, 39, L08805, <https://doi.org/10.1029/2012GL051298>, 2012.
- Tremoy, G., Vimeux, F., Soumana, S., Souley, I., Risi, C., Favreau, G., and Oi, M.: Clustering mesoscale convective systems with laser-based water vapor $\delta^{18}\text{O}$ monitoring in Niamey (Niger), *J. Geophys. Res.-Atmos.*, 119, 5079–5103, <https://doi.org/10.1002/2013JD020968>, 2014.
- Wang, H., Fyke, J. G., Lenaerts, J. T. M., Nusbaumer, J. M., Singh, H., Noone, D., Rasch, P. J., and Zhang, R.: Influence of sea-ice anomalies on Antarctic precipitation using source attribution in the Community Earth System Model, *The Cryosphere*, 14, 429–444, <https://doi.org/10.5194/tc-14-429-2020>, 2020.
- Weng, Y., Touzeau, A., and Sodemann, H.: Correcting the impact of the isotope composition on the mixing ratio dependency of water vapour isotope measurements with cavity ring-down spectrometers, *Atmos. Meas. Tech.*, 13, 3167–3190, <https://doi.org/10.5194/amt-13-3167-2020>, 2020.
- Worden, J., Noone, D., and Bowman, K.: Importance of rain evaporation and continental convection in the tropical water cycle, *Nature*, 445, 528–532, <https://doi.org/10.1038/nature05508>, 2007.